Available online at www.sciencedirect.com
ScienceDirect
Journal of Computational Physics 217 (2006) 340–363
JOURNAL OF COMPUTATIONAL PHYSICS
www.elsevier.com/locate/jcp

A spatial high-order hexahedral discontinuous Galerkin method to solve Maxwell's equations in time domain

G. Cohen [a], X. Ferrieres [b,*], S. Pernet [b]

[a] *INRIA, Domaine ds Voluceau, Rocquencourt – BP 105, 78153 Le Chesnay Cedex, France*
[b] *ONERA DEMR, unité CDE, 2 Avenue Edouard Belin, 31055 Toulouse, France*

Received 19 May 2005; received in revised form 10 November 2005; accepted 4 January 2006
Available online 24 February 2006

Abstract

In this paper, we present a non-dissipative spatial high-order discontinuous Galerkin method to solve the Maxwell equations in the time domain. The non-intuitive choice of the space of approximation and the basis functions induce an important gain for mass, stiffness and jump matrices in terms of memory. This spatial approximation, combined with a leapfrog scheme in time, leads also to a fast explicit and accurate method. A study of the dispersive error is carried out and a stability condition for the proposed scheme is established. Some comparisons with other schemes are presented to validate the new scheme and to point out its advantages. Finally, in order to improve the efficiency of the method in terms of CPU time on general unstructured meshes, a strategy of local time-stepping is proposed.

Keywords: Numerical methods; Discontinuous Galerkin methods; Maxwell's equations in time domain; Conservative spatial centered scheme; Dispersive error; Stability analysis; Local time step

1. Introduction

The most widely used method for solving Maxwell's equations in the time domain is the finite difference time domain method (FDTD) based on the well-known scheme of Yee [1] and Taflove and Hagness [2]. This method involves an orthogonal Cartesian grid and is based on a second order leapfrog approximation in space and time. However, the FDTD method suffers a certain number of limitations such as, for example, difficulty in the treatment of curved objects. In such a case, the staircase approximation can generate spurious diffraction phenomena, which strongly damage the accuracy of the solution [3].

Numerous researchers and engineers have tried to develop efficient methods, which make it possible to take into account the complex shape of objects [4–9]. Moreover, the growing need to accurately model the propagation of electromagnetic waves over a large number of wavelengths (more than 100) has forced

* Corresponding author. Tel.: +33 05 62 25 28 02; fax: +33 05 62 25 25 77.
E-mail address: ferriere@onecert.fr (X. Ferrieres).

0021-9991/$ - see front matter
doi:10.1016/j.jcp.2006.01.004

them to develop high-order or spectral methods [16,10,12]. Their first choice naturally turned towards finite element methods (FEM), which are a powerful tool for developing new numerical techniques [13]. However, one of the difficulties encountered in using finite element for Maxwell's equations is that of constructing a finite dimensional subspace of the continuous space $H(curl,\Omega)$. This functional space is natural for the solution of this problem, because the tangential components of a function belonging to $H(curl,\Omega)$ are continuous across any surface and the normal components of the same function may be discontinuous. It is well known that the use of classical continuous Langrage finite elements, which provide a suitable approximation of the space $[H^1(\Omega)]^3$, leads to spurious solutions. The appropriate finite element space – of so called edge element – was introduced by Nédélec in the 1980s [14,15]. Unfortunately, the classical version of these elements leads to a high computational cost since a matrix inversion is required at each time-step. This drawback increases with the order of approximation. Mass-lumping techniques seemed to be the right approach to avoid this inversion. An attractive method based on Nédélec's second family of edge elements was introduced by Cohen and Monk [16]. In this method, the use of the Gauss–Lobatto quadrature formulas yields a block-diagonal mass matrix, which enables us to obtain an explicit scheme for polynomial approximation at all orders. Unfortunately, this method produces important parasitic waves for large distortions of the cells. In the same idea, first and second order tetrahedral mass-lumped edge elements, which have no parasitic wave problems, were constructed in [17]. However, this approach seems to be efficient only for second-order elements.

The second choice is the use of discontinuous Galerkin methods (DGM). These methods were introduced in the first half of the 1970s by Reed and Hill [18] for the scalar neutron transport equation. Following this first study, many DGM were developed and analyzed by a large number of researchers in order to solve a large range of problems. One can find in [19] an exhaustive review of these methods from their beginning. In this survey, one can notice that few papers are devoted to the resolution of Maxwell's equations. In fact, the use of this kind of method to solve this problem is relatively recent. For the frequency domain, one can quote [21,20] and, for the time domain, one can quote [22,23,12] among numerous other papers. The main drawback of these methods is the large number of unknowns in each cell for high-order approximation schemes, which implies that much memory is needed for the local matrices (the mass matrix for example). Thus, in order to be efficient, the order of approximation in these methods must be limited. Hesthaven and Warburton [12] recently developed a low-storage, high-order, discontinuous Galerkin method for tetrahedral meshes with a judicious choice of the location of the degrees of freedom. However, his approach provides an algorithm that is $O(r^6)$ instead of $O(r^4)$ for hexahedra, r being the order of the method. One can notice that, before the use of these high-order methods, finite volume methods (that can be viewed as low order DGM schemes) were used to solve the Maxwell equations but these methods suffer from the presence of dissipation [24] or dispersion [26], which makes their use inaccurate for large-sized problems.

There are two approaches for implementing the discontinuous Galerkin methods: the h-version and the p-version. The h-version uses mesh refinement to achieve convergence to a fixed order, which keep the polynomial degree of the approximation fixed. The alternative p-version allows the order of polynomials to increase on a fixed mesh. A hybrid h–p version can also be considered. This paper concerns a method which takes to the third point of view and which enables us to reduce the storage requirement for local matrices, even for high-order approximation.

The outline of the paper is as follows. In Section 2, we describe a discontinuous Galerkin formulation for solving Maxwell's equations. In Section 3, we present some comparisons with other methods to validate this method and to show its advantages over other methods. Finally, in Section 4, a local time-stepping technique is proposed to enhance the performance of the method in terms of computational time.

2. The continuous formulation

2.1. The continuous problem

Let Ω be a domain on which the electric and magnetic fields $(\mathbf{E},\mathbf{H})$ satisfy:

$$\begin{cases} \varepsilon \frac{\partial \mathbf{E}}{\partial t} + \sigma \mathbf{E} = \nabla \times \mathbf{H}, \\ \mu \frac{\partial \mathbf{H}}{\partial t} = -\nabla \times \mathbf{E}, \\ \mathbf{E}(t=0) = 0, \quad \mathbf{H}(t=0) = 0. \end{cases} \tag{1}$$

On the boundary $\partial\Omega$ of the domain, we impose $\mathbf{n} \times \mathbf{E} = 0$ for cavity problems. This condition is also applied after PML [29] to simulate unbounded domains.

2.2. Definition of the discontinuous Galerkin framework

Let a set $\mathscr{T}_h$ of hexahedral elements $(K_i)_{i=1,N}$ be a partition of Ω. In our approach, Maxwell's equations are rewritten by adding two terms – which are equal to zero for the continuous problem – to each equation of (1). These terms define jumps of the electric and magnetic tangential components fields across the hexahedron K_i.

On each $K \in \mathscr{T}_h$, we get

$$\begin{cases} \varepsilon \frac{\partial \mathbf{E}}{\partial t} + \sigma \mathbf{E} = \nabla \times \mathbf{H} + \alpha [\![\mathbf{H} \times \mathbf{n}]\!]_{\partial K}^{K} \delta_{\partial K} + \beta [\![\mathbf{n} \times (\mathbf{E} \times \mathbf{n})]\!]_{\partial K}^{K} \delta_{\partial K}, \\ \mu \frac{\partial \mathbf{H}}{\partial t} = -\nabla \times \mathbf{E} + \gamma [\![\mathbf{E} \times \mathbf{n}]\!]_{\partial K}^{K} \delta_{\partial K} + \delta [\![\mathbf{n} \times (\mathbf{H} \times \mathbf{n})]\!]_{\partial K}^{K} \delta_{\partial K}, \end{cases} \tag{2}$$

where $[\![\mathbf{u}]\!]_{\partial K}^{K}$ defines the jump across the boundary ∂K of the volume K. More precisely, the jump is given by $[\![\mathbf{u}]\!]_{\partial K}^{K} = \mathbf{u}_K^+ - \mathbf{u}_K$ where $\mathbf{u}_K$ is the boundary value taken inside the volume K and $\mathbf{u}_K^+$ the same boundary value taken inside the other volume adjacent to ∂K. When $\Gamma = \partial K \cap \partial\Omega \neq \emptyset$, then $(\mathbf{u}_K^+)_{|\Gamma} = 0$. The term $\delta_{\partial K}$ is the Kronecker symbol for ∂K which is equal to 1 on ∂K and 0 elsewhere. It denotes the fact that these jump terms are added exclusively on the boundary of the elements. Now, we have to choose α, β, γ and δ so that (1) and (2) are equivalent problems.

Let the energy be defined by $\int_\Omega \varepsilon \mathbf{E} \cdot \mathbf{E} \, dx + \int_\Omega \mu \mathbf{H} \cdot \mathbf{H} \, dx$. For (1), this energy is constant when $\sigma = 0$. Now, we would like (2) also to satisfy an energy conservation principle. By using a weak formulation of Eqs. (2) when $\sigma = 0$, we can write for each element $K \in \mathscr{T}_h$:

$$\begin{cases} \int_K \mu \frac{\partial \mathbf{H}}{\partial t} \cdot \mathbf{H} \, dx = -\int_K \nabla \times \mathbf{E} \cdot \mathbf{H} \, dx + \gamma \int_{\partial K} [\![\mathbf{E} \times \mathbf{n}]\!]_{\partial K}^{K} \cdot \mathbf{H} \, ds + \delta \int_{\partial K} [\![\mathbf{n} \times (\mathbf{H} \times \mathbf{n})]\!]_{\partial K}^{K} \cdot \mathbf{H} \, ds, \\ \int_K \varepsilon \frac{\partial \mathbf{E}}{\partial t} \cdot \mathbf{E} \, dx = \int_K \nabla \times \mathbf{H} \cdot \mathbf{E} \, dx + \alpha \int_{\partial K} [\![\mathbf{H} \times \mathbf{n}]\!]_{\partial K}^{K} \cdot \mathbf{E} \, ds + \beta \int_{\partial K} [\![\mathbf{n} \times (\mathbf{E} \times \mathbf{n})]\!]_{\partial K}^{K} \cdot \mathbf{E} \, ds. \end{cases} \tag{3}$$

By adding the two equations over all the elements K and by integrating by part, we obtain:

$$\begin{aligned} &\sum_{K \in \mathscr{T}_h} \left(\int_K \varepsilon \frac{\partial \mathbf{E}}{\partial t} \cdot \mathbf{E} \, dx + \int_K \mu \frac{\partial \mathbf{H}}{\partial t} \cdot \mathbf{H} \, dx \right) \\ &\quad = \sum_{K \in \mathscr{T}_h} \int_{\partial K} (1 + \alpha - \gamma)(\mathbf{E}_K \times \mathbf{n}) \cdot \mathbf{H}_K \, ds - \sum_{\partial K \in \mathscr{F}_h^i} \int_{\partial K} \delta((\mathbf{E}_K + \mathbf{E}_K^+) \times \mathbf{n} \cdot (\mathbf{E}_K + \mathbf{E}_K^+) \times \mathbf{n}) \, ds \\ &\qquad + \sum_{\partial K \in \mathscr{F}_h^i} \int_{\partial K} \beta((\mathbf{H}_K + \mathbf{H}_K^+) \times \mathbf{n} \cdot (\mathbf{H}_K + \mathbf{H}_K^+) \times \mathbf{n}) \, ds + \sum_{\partial K \in \mathscr{F}_h^i} \int_{\partial K} (\alpha + \gamma)(\mathbf{E}_K^+ \times n \cdot \mathbf{H}_K + \mathbf{H}_K^+ \times \mathbf{n} \cdot \mathbf{E}_K) \, ds \\ &\qquad - \sum_{\partial K \in \mathscr{F}_h^b} \int_{\partial \hat{K}} (\delta(\mathbf{E}_K \times \mathbf{n} \cdot \mathbf{E}_K \times \mathbf{n}) + \beta(\mathbf{H}_K \times \mathbf{n} \cdot \mathbf{H}_K \times \mathbf{n})) \, ds, \end{aligned} \tag{4}$$

where $\mathscr{F}_h^i$ and $\mathscr{F}_h^b$ define, respectively, the faces inside the computational domain Ω and the faces of the boundary $\partial\Omega$.

To derive

$$\int_\Omega \varepsilon \frac{\partial \mathbf{E}}{\partial t} \mathbf{E} \, dx + \int_\Omega \mu \frac{\partial \mathbf{H}}{\partial t} \mathbf{H} \, dx = 0,$$

from Eq. (4), the values α, β, δ and γ must be such that $\beta = \delta = 0$, $1 + \alpha - \gamma = 0$ and $\alpha + \gamma = 0$ on faces belong to $\mathscr{F}_h^i$. On the other faces, energy conservation is ensured only if $\beta = \delta = 0$ and $1 + \alpha - \gamma = 0$. Hence, to guarantee energy conservation, we obtain $-\alpha = \gamma = \frac{1}{2}$ for faces belonging to $\mathscr{F}_h^i$ and we have different possibilities for α and γ for faces belonging to $\mathscr{F}_h^b$. For theses faces, our choice is guided by the equivalence between

problems (1) and (2). In particular, we set these coefficients in problem (2) so that boundary conditions of problem (1) are correctly taken into account. For example, in the case of a metallic boundary condition $\mathbf{E}_{|\partial\Omega}\times\mathbf{n}=0$ on a face in (1), we take $\gamma=1$ and then $\alpha=0$ on this face in (2) to have equivalence between the two problems.

So, an equivalent conservative formulation of (1) in each volume $K\in\mathscr{T}_h$ is given by

$$\begin{cases}\varepsilon\frac{\partial\mathbf{E}}{\partial t}+\sigma\mathbf{E}=\nabla\times\mathbf{H}+\alpha[\![\mathbf{H}\times\mathbf{n}]\!]^K_{\partial K}\delta_{\partial K},\\ \mu\frac{\partial\mathbf{H}}{\partial t}=-\nabla\times\mathbf{E}+\gamma[\![\mathbf{E}\times\mathbf{n}]\!]^K_{\partial K}\delta_{\partial K},\end{cases}\tag{5}$$

with the values of α and γ as previously defined.

3. Construction of the approximation

3.1. Approximate formulation

For the following of this paper, we assume each cell K in the $\mathscr{T}_h$ partition to be constituted by a homogeneous material, where the electric and magnetic fields are sufficiently regular to be considered in $(H^1(K))^3$. In order to define an approximation (5), we must first introduce the space

$$\boldsymbol{H}^1(\mathscr{T}_h)=\left\{\boldsymbol{v}\in(L^2(\Omega))^3;\forall K\in\mathscr{T}_h,\boldsymbol{v}_{|K}\in(H^1(K))^3\right\}.$$

Then, we can define the following variational formulation of (5).

Find $(\mathbf{E},\mathbf{H})\in(\boldsymbol{H}^1(\mathscr{T}_h))^2$ such that

$$\begin{cases}\varepsilon\frac{\partial}{\partial t}\int_\Omega\mathbf{E}\cdot\boldsymbol{\varphi}\,dx=-\int_\Omega\sigma\mathbf{E}\cdot\boldsymbol{\varphi}\,dx+\sum\limits_{K\in\mathscr{T}_h}\int_K\nabla\times\mathbf{H}\cdot\boldsymbol{\varphi}\,dx+\sum\limits_{K\in\mathscr{T}_h}\alpha\int_{\partial K}[\![\mathbf{H}\times\mathbf{n}]\!]^K_{\partial K}\cdot\boldsymbol{\varphi}\,ds,\\ \mu\frac{\partial}{\partial t}\int_\Omega\mathbf{H}\cdot\boldsymbol{\psi}\,dx=\sum\limits_{K\in\mathscr{T}_h}\left(-\int_K\nabla\times\mathbf{E}\cdot\boldsymbol{\psi}\,dx+\gamma\int_{\partial K}[\![\mathbf{E}\times\mathbf{n}]\!]\cdot\boldsymbol{\psi}\,ds\right),\end{cases}\tag{6}$$

where $\boldsymbol{\varphi}\in\boldsymbol{H}^1(\mathscr{T}_h)$ and $\boldsymbol{\psi}\in\boldsymbol{H}^1(\mathscr{T}_h)$.

In a second step, we define the approximation space of $\boldsymbol{H}^1(\mathscr{T}_h)$:

$$U_h=\left\{\boldsymbol{v}\in(L^2(\Omega))^3;\forall K\in\mathscr{T}_h,DF_K^*\boldsymbol{v}_{|K}oF_K\in[Q_r(\hat{K})]^3\right\},$$

where $Q_r(\hat{K})$ is the set of polynomials of $\hat{K}=[0,1]^3$ whose order is less or equal to r in each variable. For any $K\in\mathscr{T}_h$, $\boldsymbol{F}_K$ is the conform mapping such that $\boldsymbol{F}_K(\hat{K})=K$ and DF_K the Jacobian matrix of $\boldsymbol{F}_K$. In the following, we shall denote $J_K=\det(DF_K)$ the Jacobian of $\boldsymbol{F}_K$. The definition of the approximate space U_h is not classical for discontinuous Galerkin methods (generally the solution is approximate by a polynom on each cell), but, as we shall see later, the use of the curl-conforming mapping in our approximation will be important to imply a low storage for the stiffness and jump matrices and a substantial gain on CPU time.

In this space, the following approximate formulation holds:

Find $(\mathbf{E}_h,\mathbf{H}_h)\in(U_h)^2$ such that

$$\begin{cases}\varepsilon\frac{\partial}{\partial t}\int_\Omega\mathbf{E}_h\cdot\boldsymbol{\varphi}_h\,dx=-\int_\Omega\sigma\mathbf{E}_h\cdot\boldsymbol{\varphi}_h\,dx+\sum\limits_{K\in\mathscr{T}_h}\int_K\nabla\times\mathbf{H}_h\cdot\boldsymbol{\varphi}_h\,dx+\sum\limits_{K\in\mathscr{T}_h}\alpha\int_{\partial K}[\![\mathbf{H}_h\times\mathbf{n}]\!]^K_{\partial K}\cdot\boldsymbol{\varphi}_h\,ds,\\ \mu\frac{\partial}{\partial t}\int_\Omega\mathbf{H}_h\cdot\boldsymbol{\psi}_h\,dx=\sum\limits_{K\in\mathscr{T}_h}\left(-\int_K\nabla\times\mathbf{E}_h\cdot\boldsymbol{\psi}_h\,dx+\gamma\int_{\partial K}[\![\mathbf{E}_h\times\mathbf{n}]\!]\cdot\boldsymbol{\psi}_h\,ds\right).\end{cases}\tag{7}$$

3.2. Basis functions and degrees of freedom

3.2.1. Basis functions on the unit cube

In order to define the basis functions of U_h, we first define the basis functions on the unit cube $\hat{K}$ (Fig. 1). Let $\vec{\hat{\xi}}_{ijk}=(\hat{\xi}_i,\hat{\xi}_j,\hat{\xi}_k)$, $1\leqslant i\leqslant r+1$, $1\leqslant j\leqslant r+1$, $1\leqslant k\leqslant r+1$, be a set of points of $\hat{K}$, where $\hat{\xi}_\ell$ represents the abscissa of a Gauss quadrature point on the interval $[0,1]$. On the other hand, we define the set of the $(r+1)^3$

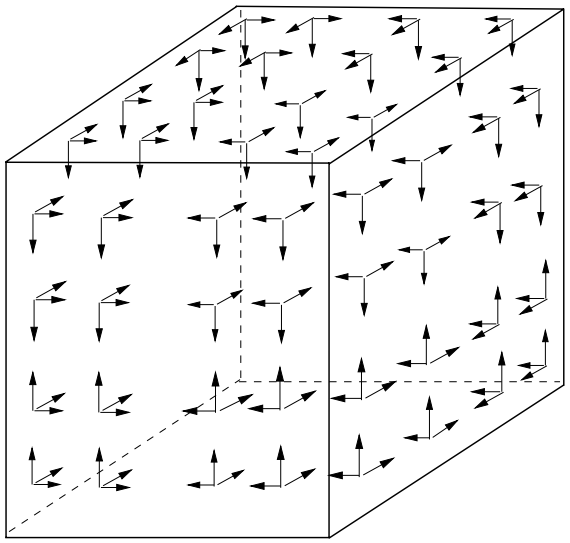

Fig. 1. Basis functions located on the unit cube for a Q_3 approximation.

Lagrange interpolation polynomials $\hat{\varphi}_{ijk} \in Q_r$ such that $\hat{\varphi}_{ijk}(\vec{\hat{\xi}}_{\ell,m,n}) = \delta_{i\ell}\delta_{jm}\delta_{kn}$, where δ_{ij} is the Kronecker symbol. We finally define the following set $\widehat{\mathscr{B}}$ of $3(r+1)^3$ vector-valued functions basis functions on $\hat{K}$: $\hat{\boldsymbol{\varphi}}^{(1)}_{ijk} = (\hat{\varphi}_{ijk}, 0, 0)^{\mathrm{T}}$, $\hat{\boldsymbol{\varphi}}^{(2)}_{ijk} = (0, \hat{\varphi}_{ijk}, 0)^{\mathrm{T}}$, $\hat{\boldsymbol{\varphi}}^{(3)}_{ijk} = (0, 0, \hat{\varphi}_{ijk})^{\mathrm{T}}$.

3.2.2. Basis functions on any hexahedron K

Following the definition of U_h, we can now deduce from $\widehat{\mathscr{B}}$ a basis $\mathscr{B}$ of this space. On each element K, we define a set of $3(r+1)^3$ basis functions $\boldsymbol{\varphi}^{(\ell)}_{ijk,K}$ such that $\boldsymbol{\varphi}^{(\ell)}_{ijk,K} = DF_K^{*-1}\hat{\boldsymbol{\varphi}}^{(\ell)}_{ijk}$, for all $\ell = 1, \ldots, 3$. So,

$$\mathscr{B} = \left\{ \boldsymbol{\varphi}^{(\ell)}_{ijk,K}, \forall K \in \mathscr{T}_h, \forall (ijk) \in \{1, \ldots, r+1\}^3, \forall \ell \in \{1,2,3\} \right\}.$$

In their definition, the L^2-character of the functions implies that the support of each basis function is reduced to one element. Thus, it is obvious that $\dim U_h = 3(r+1)^3 N_e$ for any mesh whose number of elements is N_e.

3.2.3. Mass matrices

In the weak formulation, we need to evaluate for each basis function $\boldsymbol{\varphi}^l_{ijk,K}(x)$ the discrete form of the terms $\int_\Omega \mathbf{E}(t,x) \cdot \boldsymbol{\varphi}^l_{ijk,K}(x)\,\mathrm{d}x$, $\int_\Omega \mathbf{H}(t,x) \cdot \boldsymbol{\varphi}^l_{ijk,K}(x)\,\mathrm{d}x$ and $\int_\Omega \sigma(x)\mathbf{E}(t,x) \cdot \boldsymbol{\varphi}^l_{ijk,K}(x)\,\mathrm{d}x$. These three integrals have a similar relation between basis functions and we apply the same developments to evaluate them.

So, we only explain how to obtain the discrete form of $\int_\Omega \mathbf{E}(t,x) \cdot \boldsymbol{\varphi}^l_{ijk,K}(x)\,\mathrm{d}x$.

By using $\mathbf{E}(x,t) o F_K = \sum_{K \in \mathscr{T}_h} \sum_{l=1}^{3} \sum_{i,j,k=1,r+1} E^l_{ijk,K}(t) (DF^*_K(\hat{x}))^{-1} \hat{\boldsymbol{\varphi}}^l_{ijk}(\hat{x})$ we can write

$$\int_\Omega \mathbf{E}(t,x) \cdot \boldsymbol{\varphi}^l_{ijk,K}(x)\,\mathrm{d}x = \int_K \mathbf{E}(t,x) \cdot \boldsymbol{\varphi}^l_{ijk,K}(x)\,\mathrm{d}x,$$

since $K = \mathrm{Supp}(\boldsymbol{\varphi}^l_{ijk,K})$.

So, we obtain

$$\begin{aligned}
\int_K \mathbf{E}(t,x) \cdot \boldsymbol{\varphi}^l_{ijk,K}\,\mathrm{d}x &= \sum_{p=1}^{3} \sum_{m,n,q=1,N} E^p_{mnq,K}(t) \int_{\hat{K}} (DF^*_K)^{-1}(\hat{x}) \hat{\boldsymbol{\varphi}}^p_{mnq}(\hat{x}) \cdot (DF^*_K)^{-1}(\hat{x}) \hat{\boldsymbol{\varphi}}^l_{ijk}(\hat{x}) |J_K(\hat{x})|\,\mathrm{d}\hat{x} \\
&= \sum_{p=1}^{3} \sum_{m,n,q=1,N} E^p_{mnq,K}(t) \int_{\hat{K}} DF_K^{-1}(\hat{x}) (DF^*_K)^{-1}(\hat{x}) \hat{\boldsymbol{\varphi}}^p_{mnq}(\hat{x}) \cdot \hat{\boldsymbol{\varphi}}^l_{ijk}(\hat{x}) |J_K(\hat{x})|\,\mathrm{d}\hat{x}.
\end{aligned}$$

By using the Gauss quadrature rule for the integral and the fact that $\hat{\boldsymbol{\varphi}}^l_{ijk}(\hat{x}_{mnq}) = \delta_i(\hat{x}_m)\delta_j(\hat{y}_n)\delta_k(\hat{z}_q)$, we finally get

$$\int_K \mathbf{E}(t,x)\cdot\boldsymbol{\varphi}^l_{ijk,K}\mathrm{d}x = \omega_{ijk}\sum_{p=1}^{3} E^p_{ijk,K}(DF_K^{-1}(\hat{x}_{ijk})(DF_K^*)^{-1}(\hat{x}_{ijk}))_{pl}|J_K(\hat{x}_{ijk})|$$

where ω_{ijk} is the quadrature weight at the point $\hat{x}_{ijk}$ and $(M)_{pl}$ defines the (p,l) term in the matrix M.

So, in the matrix of the discrete problem for a degree of freedom, we have three non-zero terms for the basis function which are defined at the same given quadrature point. By choosing a numbering of the unknowns around the points, we obtain a 3×3 block-diagonal mass matrix which can be diagonal for regular elements.

3.2.4. Stiffness matrix

The terms of the weak formulation considered here are $\int_\Omega \nabla\times E(t,x)\cdot\boldsymbol{\varphi}^l_{ijk,K}(x)\,\mathrm{d}x$ for the electric equation and $\int_\Omega \nabla\times H(t,x)\cdot\boldsymbol{\varphi}^l_{ijk,K}(x)\,\mathrm{d}x$ for the magnetic equation. As in the previous section, we explain only the construction of the discrete form of the term related to the electric equation. A similar demonstration holds for the magnetic equation related terms. As for the evaluation of the mass matrix, we have

$$\int_\Omega \nabla\times E(t,x)\cdot\boldsymbol{\varphi}^l_{ijk,K}(x)\,\mathrm{d}x = \int_K \nabla\times E(t,x)\cdot\boldsymbol{\varphi}^l_{ijk,K}(x)\,\mathrm{d}x,$$

where K is the unique element on which $\boldsymbol{\varphi}^l_{ijk,K}(x)$ is not identically equal to zero.

$$\begin{aligned}
\int_K \nabla\times E(t,x)\cdot\boldsymbol{\varphi}^l_{ijk,K}(x)\,\mathrm{d}x &= \int_{\hat{K}} ((DF^*)^{-1}(\hat{x})\hat{\nabla})\times((DF^*)^{-1}(\hat{x})\hat{E}(t,\hat{x}))\cdot(DF^*)^{-1}(\hat{x})\hat{\boldsymbol{\varphi}}^l_{ijk}(\hat{x})|J(\hat{x})|\,\mathrm{d}\hat{x}\\
&= \int_{\hat{K}} \frac{DF(\hat{x})}{J(\hat{x})}(\hat{\nabla}\times\hat{E}(t,\hat{x}))\cdot(DF^*)^{-1}(\hat{x})\hat{\boldsymbol{\varphi}}^l_{ijk}|J(\hat{x})|\,\mathrm{d}\hat{x}\\
&= \int_{\hat{K}} \mathrm{sign}(J(\hat{x}))(\hat{\nabla}\times\hat{E}(t,\hat{x}))\cdot\hat{\boldsymbol{\varphi}}^l_{ijk}(\hat{x})\,\mathrm{d}\hat{x}\\
&= \sum_{m,n,q=1,N}\sum_{p=1}^{3}\mathrm{sign}(J(\hat{x}))\int_{\hat{K}} E^p_{mnq,K}(t)(\hat{\nabla}\times\hat{\boldsymbol{\varphi}}^p_{mnq}(\hat{x}))\cdot\hat{\boldsymbol{\varphi}}^l_{ijk}(\hat{x})\,\mathrm{d}\hat{x}\\
&= \sum_{m,n,q=1,N}\sum_{p=1}^{3}\mathrm{sign}(J(\hat{x}_{mnq}))\omega_{mnq}E^l_{mnq,K}(t)(\hat{\nabla}\times\hat{\boldsymbol{\varphi}}^p_{mnq})^l(\hat{x}_{ijk}),
\end{aligned}$$

where $(\nabla\times u)^l$ is the l component of $\nabla\times u$.

We can see on this formula that, for all given elements K, the stiffness matrix is obtained only by the knowledge of the derivative term $\hat{\nabla}\times\hat{\boldsymbol{\varphi}}^l_{ijk}$ for all components and points on the reference element and by the sign of the Jacobian at each point on the element K. Because we assume that the inverse of the Jacobian always exists, the sign of the Jacobian must be the same on the element. So we only need to know the sign of the Jacobian at a given point on each element to have it for all points on the element. Then, for the stiffness matrix, we only need to store the derivative terms on the reference element and a sign for each element K. This implies a very small storage and a fast process to obtain the full stiffness matrix of the scheme.

3.2.5. Jump matrix

We denote the set of faces of $\mathscr{T}_h$ by $\mathscr{F}_h = \mathscr{F}^i_h \cup \mathscr{F}^b_h$, where $\mathscr{F}^i_h = \{\Gamma\in\mathscr{F}^i_h, \Gamma = K'\cap K\}$ and $\mathscr{F}^b_h = \{\Gamma\in\mathscr{F}^b_h, \Gamma = K\cap\partial\Omega\}$ are the sets of the interior and boundary faces.

The computation of the jump or flux terms is one of the most expensive parts in the time domain algorithms using finite volume or discontinuous Galerkin spatial approximation. An inappropriate computational approach or a bad formulation can dramatically penalize the computational code. We will see that the approximate space as well as the DGM formulation used leads to an efficient computation of the jump terms. Actually, a detailed computation of these terms will show that they need a negligible storage. Moreover, we will see that the number of operations to determine these terms is dramatically reduced, thanks to the correspondence of the basis functions with the selected quadrature points.

Let $\boldsymbol{\varphi}^l_{ijk,K}$ be a basis function defined by $\boldsymbol{\varphi}^l_{ijk,K} o F_K = DF_K^{*-1}\hat{\boldsymbol{\varphi}}^l_{ijk}$. The terms considered here are $\int_{\partial K}[\![\mathbf{H}\times\mathbf{n}]\!]\cdot\boldsymbol{\varphi}^l_{ijk,K}\,\mathrm{d}s$ and $\int_{\partial K}[\![\mathbf{E}\times\mathbf{n}]\!]\cdot\boldsymbol{\varphi}^l_{ijk,K}\,\mathrm{d}s$.

One can decompose the boundary, ∂K, of K in $\partial K = \bigcup_{i=1}^{6} \Gamma_i$, with $\Gamma_i \in \mathscr{F}$ for which $F_{K|\Gamma_i}(\hat{\Gamma}_i) = \Gamma_i$ with $\hat{\Gamma}_i \subset \partial\hat{K}$ for $i = 1, \ldots, 6$.

We can write

$$\int_{\partial K} [\![H_h \times \mathbf{n}_K]\!]_{\partial K}^{K} \cdot \boldsymbol{\varphi}_{ijk,K}^{l} \, \mathrm{d}\sigma = \sum_{i=1}^{6} \int_{\Gamma_i} [\![H_h \times \mathbf{n}_i^K]\!]_{\Gamma_i}^{K} \cdot \boldsymbol{\varphi}_{ijk,K}^{l} \, \mathrm{d}\sigma_i, \tag{8}$$

where $\mathrm{d}\sigma_i$ is the surface element of the face Γ_i and n_i^K the unit outward normal to K associated with Γ_i.

Let Γ_i be a face of K so that $\mathbf{F}_{K|\Gamma_i}(\hat{\Gamma}_i) = \Gamma_i$, we have $\mathrm{d}\sigma_i = |J_{K|\hat{\Gamma}_i}| \| DF_{K|\hat{\Gamma}_i}^{*-1} \hat{n}_i \| \, \mathrm{d}\hat{\eta}_i \, \mathrm{d}\hat{\chi}_i$ where $\hat{n}_i$ is the unit outward normal to $\hat{K}$ associated with the reference face $\hat{\Gamma}_i$ and $\hat{\eta}$, $\hat{\chi}$ are the tangential components of this face (i.e., $\hat{x}$, $\hat{y}$ or $\hat{z}$).

The definition of the basis functions also provides the following property (see [11]):

Let $\mathbf{u}_h \in U_h$, we have

$$(\mathbf{u}_{h|K} \times \mathbf{n}_i^K) o F_{K|\hat{\Gamma}_i} = \frac{1}{J_{K|\hat{\Gamma}_i} \| DF_{K|\hat{\Gamma}_i}^{*-1} \hat{\mathbf{n}}_i \|} DF_{K|\hat{\Gamma}_i} (\hat{\mathbf{u}}_{K|\hat{\Gamma}_i} \times \hat{\mathbf{n}}_i), \tag{9}$$

where $\hat{\mathbf{u}}_K = \sum_{l=1}^{3} \sum_{i,j,k}^{r+1} u_{ijk}^l \hat{\boldsymbol{\varphi}}_{ijk}^l$ and $\mathbf{n}_i^K$ is the unit outward normal to K associated with the face Γ_i.

By using these two previous properties, we can prove the following proposition:

Proposition 1. *$\forall \Gamma_i \in \mathscr{F}_h^b$, we have*

$$\int_{\Gamma_i} [\![\mathbf{H}_h \times \mathbf{n}_i]\!]_{\Gamma_i}^{K} \cdot \boldsymbol{\varphi}_{ijk}^{l} \, \mathrm{d}\sigma_i = -\mathrm{sign}(J_K) \int_{\hat{\Gamma}_i} (\hat{\mathbf{H}}_{K|\hat{\Gamma}_i} \times \hat{\mathbf{n}}_i) \cdot \hat{\boldsymbol{\varphi}}_{ijk}^{l} \, \mathrm{d}\hat{\eta}_i \, \mathrm{d}\hat{\chi}_i. \tag{10}$$

In this proposition, evaluating the term $\int_{\hat{\Gamma}_i} (\hat{\mathbf{H}}_{K|\hat{\Gamma}_i} \times \hat{n}_i) \cdot \hat{\boldsymbol{\varphi}}_{ijk}^{l} \, \mathrm{d}\hat{\eta}_i \, \mathrm{d}\hat{\chi}_i$ needs a very small number of operations. Take for example a face $\hat{\Gamma}_i = \{\hat{z} = 0\}$, we obtain by using a Gauss quadrature rule:

- if $l = 3$, then $\int_{\hat{\Gamma}_i} (\hat{\mathbf{H}}_{K|\hat{\Gamma}_i} \times \hat{\mathbf{n}}_i) \cdot \hat{\boldsymbol{\varphi}}_{ijk}^{l} \, \mathrm{d}\hat{x}_1 \, \mathrm{d}\hat{x}_2 = 0$,
- if $l = 1$, then $\int_{\hat{\Gamma}_i} (\hat{\mathbf{H}}_{K|\hat{\Gamma}_i} \times \hat{\mathbf{n}}_i) \cdot \hat{\boldsymbol{\varphi}}_{ijk}^{l} \, \mathrm{d}\hat{x}_1 \mathrm{d}\hat{x}_2 = -\sum_{l_3=1}^{r+1} H_{ijl_3,K}^{2} \hat{\omega}_i \hat{\omega}_j \hat{\varphi}_{l_3}(0) \hat{\varphi}_k(0)$,
- if $l = 2$, then $\int_{\hat{\Gamma}_i} (\hat{\mathbf{H}}_{K|\hat{\Gamma}_i} \times \hat{\mathbf{n}}_i) \cdot \hat{\boldsymbol{\varphi}}_{ijk}^{l} \, \mathrm{d}\hat{x}_1 \, \mathrm{d}\hat{x}_2 = \sum_{l_3=1}^{r+1} H_{ijl_3,K}^{1} \hat{\omega}_i \hat{\omega}_j \hat{\varphi}_{l_3}(0) \hat{\varphi}_k(0)$,

where $\{\hat{\omega}_i, \hat{\omega}_j\}_{l,m=1,\ldots,r+1}$ are the quadrature weights.

One has the same type of results for all the other faces of reference. One can see that the computation of the surface term coming from a boundary face requires little storage. Indeed, only the sign of Jacobian and negligible basis functions interactions on the reference faces must be known. Finally, the previous expressions show that the number of interactions between the basis functions is limited (only $r_k + 1$ interactions). This induces a substantial gain of CPU time for the computation of these quantities.

Now, we are going to see that the same conclusions are reached when computing the jump terms for the interior faces.

Let $\Gamma_i \in \mathscr{F}_h^i$ where $\Gamma_i = K \cap K'$, then we have

$$\int_{\Gamma_i} [\![H_h \times \mathbf{n}_i]\!]_{\Gamma_i}^{K} \cdot \boldsymbol{\varphi}_{ijk,K}^{l} \, \mathrm{d}\sigma_i = \int_{\hat{\Gamma}_i} |J_{K|\hat{\Gamma}_i}| \| DF_{K|\hat{\Gamma}_i}^{*-1} \hat{\mathbf{n}}_i \| (\mathbf{H}_{hK'} \times \mathbf{n}_i - \mathbf{H}_{hK} \times \mathbf{n}_i) o F_{K|\hat{\Gamma}_i} \cdot DF_K^{*-1} \hat{\boldsymbol{\varphi}}_{ijk}^{l} \, \mathrm{d}\hat{\eta}_i \, \mathrm{d}\hat{\chi}_i. \tag{11}$$

In (11), the computation of the part of the integral containing $\mathbf{H}_{hK}$ is done in the same way as for a boundary face. So, the previous proposition can be applied to this case and we obtain the same conclusions. Thus, we are only interested in the $\mathbf{H}_{hK'}$ term, i.e.,

$$I = \int_{\hat{\Gamma}_i} |J_{K|\hat{\Gamma}_i}| \| DF_{K|\hat{\Gamma}_i}^{*-1} \hat{\mathbf{n}}_i \| (\mathbf{H}_{hK'} \times \mathbf{n}_i) \cdot DF_K^{*-1} \hat{\boldsymbol{\varphi}}_{ijk}^{l} \, \mathrm{d}\hat{\eta}_i \, \mathrm{d}\hat{\chi}_i. \tag{12}$$

Let $i' \in \{1, \ldots, 6\}$ such that: $F_{K'}(\hat{\Gamma}_{i'}) = F_K(\hat{\Gamma}_i) = \Gamma_{i'} = \Gamma_i$. Let us consider the following change of variables:

$$\mathscr{G}_{K' \to K} = F_{K|\Gamma_i}^{-1} o F_{K'|\hat{\Gamma}_{i'}} : \hat{\Gamma}_{i'} \to \hat{\Gamma}_i. \tag{13}$$

Then $\forall \hat{x}' \in \hat{\Gamma}_{i'}$, we have

$$\left(|J_{K'|\hat{\Gamma}_{i'}}|\|DF^{*-1}_{K'|\hat{\Gamma}_{i'}}\hat{\mathbf{n}}_{i'}\|\right)(\hat{x}') = \left(|J_{K|\hat{\Gamma}_i}|\|DF^{*-1}_{K|\hat{\Gamma}_i}\hat{\mathbf{n}}_i\|\right) o\mathscr{G}_{K'\to K}(\hat{x}'). \tag{14}$$

The change of variables (13) and (9) gives

$$I = -\int_{\hat{\Gamma}_{i'}} \frac{\left(|J_{K|\hat{\Gamma}_i}|\|DF^{*-1}_{K|\hat{\Gamma}_i}\hat{\mathbf{n}}_i\|\right) o\mathscr{G}_{K'\to K}}{J_{K'|\hat{\Gamma}_{i'}}\|DF^{*-1}_{K'|\hat{\Gamma}_{i'}}\hat{\mathbf{n}}_{i'}\|} DF_{K'|\hat{\Gamma}_{i'}}(\hat{\mathbf{H}}_{K'|\hat{\Gamma}_{i'}} \times \hat{\mathbf{n}}_{i'}) \cdot (DF^{*-1}_K \hat{\boldsymbol{\varphi}}^l_{ijk}) o\mathscr{G}_{K'\to K}\, \mathrm{d}\hat{\eta}_{i'}\, \mathrm{d}\hat{\chi}_{i'}. \tag{15}$$

Property (14) leads to the simplification:

$$I = -\mathrm{sign}(J_{K'}) \int_{\hat{\Gamma}_{i'}} (DF^{-1}_K o\mathscr{G}_{K'\to K} DF_{K'})(\hat{\mathbf{H}}_{K'} \times \hat{\mathbf{n}}_{i'}) \cdot \hat{\boldsymbol{\varphi}}^l_{ijk} o\mathscr{G}_{K'\to K}\, \mathrm{d}\hat{\eta}_{i'}\, \mathrm{d}\hat{\chi}_{i'}. \tag{16}$$

Remark 1. $(DF^{-1}_K o\mathscr{G}_{K'\to K} DF_{K'})$ and $\mathscr{G}_{K'\to K}$ provide the connection with the local numbering of the degrees of freedom of K and K'. Both are permutation matrices constant per face.

So, in order to compute (16), it is sufficient to know the matrix $DF^{-1}_K o\mathscr{G}_{K'\to K} DF_{K'}$ on each internal face of $\mathscr{T}_h$. Its constant character implies that, to evaluate it, we only have to compute it at one point of this face.

3.2.6. Semi-discrete numerical scheme and 3D spatial dispersion analysis

In the previous sections, we described the different integral terms of the weak formulation and we showed that our choice of approximation spaces and basis functions led to a low storage algorithm, whenever using high order spatial approximations. In this section, we first give a full matrix representation of the semi-discrete numerical scheme obtained, then we provide an analysis of the spatial dispersive error of the scheme.

The semi-discrete numerical scheme proposed in this paper can be written as

$$\begin{aligned} M_\varepsilon \frac{\partial E}{\partial t} + M_\sigma E &= RH + S_E E, \\ M_\mu \frac{\partial H}{\partial t} &= -RE + S_H H \end{aligned} \tag{17}$$

where M_ε, M_μ, M_σ are 3×3 block-diagonal matrices, R is the stiffness matrix and S_E, S_H are the jump matrices whose terms are given in the previous sections. In these matrices, only the mass matrices must be stored because they depend on the element K. For the stiffness and jump matrices, we just have to store the sign of the Jacobian and a permutation matrix for each element K. Finally, in terms of storage required by the method we roughly have

- $6\times(r+1)^3$ real values per cell for the unknowns,
- $3\times 6\times(r+1)^3$ real values per cell for the mass matrices ($6\times(r+1)^3$ values for an homogeneous non-lossy experiment),
- 1 value per cell for the sign of the Jacobian,
- $4\times(r+1)^3$ values per face for the fluxes.

This implies a total storage between $24\times(r+1)^3+1$ and $36\times(r+1)^3+1$ values per cell, where r is the spatial order of the scheme.

We also choose to consider a spatial conservative numerical scheme in order to avoid errors due to numerical dissipation. To complete the analysis of our spatial scheme, let us now study the spatial dispersive error of the scheme. We prove that the 3D dispersion is deduced from the 1D one. In particular, this result allows us to easily determine the rate of convergence in space on Cartesian grid of the GD scheme studied here.

For this purpose, we consider an infinite regular mesh of $\mathbb{R}^3$ with a space-step equal to h. For $\mathbf{p} = (p_1, p_2, p_3) \in \mathbb{Z}^3$, we denote the cell $[p_1 h, (p_1+1)h]\times[p_2 h, (p_2+1)h]\times[p_3 h, (p_3+1)h]$ by $I_{\mathbf{p}}$. On this mesh, we assume that the discrete solution can be written in the form of the following numerical plane wave (see for example [11]):

$$E^l_{ijk,\mathbf{p}} = E^l_{ijk} e^{i(\omega_h t - k_1 h p_1 - k_2 h p_2 - k_3 h p_3)} e^{-i(\hat{x}_i k_1 h + \hat{y}_j k_2 h + \hat{z}_k k_3 h)},$$
$$H^l_{ijk,\mathbf{p}} = H^l_{ijk} e^{i(\omega_h t - k_1 h p_1 - k_2 h p_2 - k_3 h p_3)} e^{-i(\hat{x}_i k_1 h + \hat{y}_j k_2 h + \hat{z}_k k_3 h)}, \tag{18}$$

where $\hat{x}_i$, $\hat{y}_j$ and $\hat{z}_k$ are Gauss–Lobatto quadrature points and $l = 1,2,3$ are the three vector components.

Now, by reporting (18) into the discrete system, we get for the first electric component an equation of the form:

$$w_h h \varepsilon E^1_{ijk} = \sum_{l_3=1}^{r+1} H^2_{i,j,l_3} B_{h,r}[k_3](k,l_3) - \sum_{l_2=1}^{r+1} H^3_{i,l_2,k} B_{h,r}[k_2](j,l_2), \tag{19}$$

where $B_{h,r}[k_3](k,l_3)$ and $B_{h,r}[k_2](j,l_2)$ are geometric terms given by the discrete scheme.

Let A and B be $m \times n$ and $p \times q$ matrices, respectively. The Kronecker product is the $mp \times nq$ matrix $C = A \otimes B$ given by: $C_{(i-1)p+l,(j-1)q+r} = A_{i,j} B_{l,r}$ By using the Kronecker product, we can still write Eq. (19):

$$w_h h \varepsilon E^1 = (I_{r+1} \otimes I_{r+1} \otimes B_{h,r}[k_3]) H^2 - (I_{r+1} \otimes B_{h,r}[k_2] \otimes I_{r+1}) H^3, \tag{20}$$

where $E^l = E^l_{ijk,p}$ and $H^l = H^l_{ijk,p}$ for $l = 1,2,3$, and $i,j,k = 1,\ldots,r+1$.

By working in the same way for the other components, one obtains the matrix system:

$$\omega_h h \begin{pmatrix} \varepsilon E \\ \mu H \end{pmatrix} = \begin{pmatrix} 0 & A \\ -A & 0 \end{pmatrix} \begin{pmatrix} E \\ H \end{pmatrix}, \tag{21}$$

with $E = (E^l)_{l=1,3}$, $H = (H^l)_{l=1,3}$ and

$$A = \begin{pmatrix} 0 & a_3 & -a_2 \\ -a_3 & 0 & a_1 \\ a_2 & -a_1 & 0 \end{pmatrix}.$$

The terms a_1, a_2 and a_3 are, respectively, given by $B_{h,r}[k_1] \otimes I_{r+1} \otimes I_{r+1}$, $I_{r+1} \otimes B_{h,r}[k_2] \otimes I_{r+1}$ and $I_{r+1} \otimes I_{r+1} \otimes B_{h,r}[k_3]$ Finally, by using (21), we obtain the fundamental relations $\forall l = 1,\ldots,3$

$$\varepsilon \mu h^2 \omega_h^2 E^l = \alpha E^l,$$
$$\varepsilon \mu h^2 \omega_h^2 H^l = \alpha H^l, \tag{22}$$

where $\alpha = ((B_{h,r}[k_1])^2 \otimes I_{r+1} \otimes I_{r+1}) + (I_{r+1} \otimes (B_{h,r}[k_2])^2 \otimes I_{r+1}) + (I_{r+1} \otimes I_{r+1} \otimes (B_{h,r}[k_3])^2)$. Then, we obtain the following theorem:

Theorem 1. *Let ω_h be an eigenvalue of the spectral problem (22), then we have*

$$\omega_h^2 = \frac{1}{c^2 h^2} (\omega_h[k_1]^2 + \omega_h[k_2]^2 + \omega_h[k_3]^2), \tag{23}$$

where $\omega_h[k_i]^2$ are not only the eigenvalues of the matrix $(B_{h,r}[k_i])^2$, but also the eigenvalues of the 1D dispersion problem associated with the wavevectors k_i and $c = \frac{1}{\sqrt{\varepsilon\mu}}$.

In conclusion, the 3D dispersive properties are similar to those established in 1D. In particular, we obtain the same orders of approximation. Table 1 lists the rate of convergence ($\mathcal{O}(h^{p_r})$) obtained by using a 1D dispersion analysis of our DG approximation.

In this table, we can notice that dispersive error of the scheme decreases as the order of the scheme increases. However, these values seem to indicate that the accuracy of the scheme is the same for orders 2 and 3 and for orders 4 and 5. This is not exactly true. Indeed, we can write the dispersion error as kh^n where k, h and n are, respectively, a constant, the spatial step and the order of the scheme. For the different orders

Table 1
Numerical dispersion orders for different orders of approximation

Order of approximation	$r=1$	$r=2$	$r=3$	$r=4$	$r=5$
Order of dispersive error	2	6	6	10	10

$n = 1, 2, 3, 4, 5$, the evaluated constant k is, respectively, equal to 3.2898, −2670.1817, 312.48, −931215.53 and 47988.2293. Taking into account these constant values, we can see that order 3 (respectively, 5) is better than order 2 (respectively, 4).

The pattern of the dispersive orders obtained in Table 1, is related to the choice of the centered fluxes. A study of the dispersive errors was also made by using non-centered fluxes ($\beta = \delta = \frac{1}{2}$) with our approximation. The values obtained are shown in Table 2. These results show that the approach of the non-centered fluxes is more attractive in terms of dispersive errors, but we also have an important additional cost storage for jump matrices due to the terms $[\![n \times (E \times n)]\!]$ and $[\![n \times (H \times n)]\!]$ and the scheme becomes dissipative. In these conditions, the centered fluxes scheme of the stays to be more interesting.

3.2.7. Numerical approximation in time and stability analysis

The most natural way for time discretization would be to use higher-order finite difference schemes. Generally, such explicit schemes are unstable [27]. In the domain of centered schemes (which are not dissipative and coherent with our choice), very few alternatives remain. The stable modified equation approach or symmetric schemes are complicated and are very difficult to adapt to unbounded domain conditions such as ABC or PML [11]. For these reasons, we decided to use a simple leapfrog scheme in time. The problem is to know if this low approximation in time compared to the one in space can introduce errors, which annihilate the advantage to use spatial schemes of order higher than 2. Numerical experiments have shown that it is not the case. Although of second-order, the time scheme appeared to be accurate for relatively long time-requiring experiments ($\simeq$50 wavelengths). This is mainly due to the fact that we do not use it with its maximal CFL on non-regular meshes, in which the size of the elements can vary with a ratio of 10 or even more and the CFL is adapted to the smallest cell. Of course, for longer experiments, a phase-shift, which increases with time, can be observed.

To illustrate this purpose, Fig. 2 shows the evolution of the L^2 error for different spatial orders. We can see that increasing the order of the spatial approximation allows us to have a more accurate solution. The L^2 error defines here the L^2 norm of the difference between the exact solution and the solution computed for each degree of freedom in the problem. The configuration and the analytic solution of the example used in this figure are the same as the example proposed for the evaluation of modes inside cavity in numerical results section. Another possibility to quantitatively evaluate the accuracy of our approximation consists in seeing the ability of the scheme to restitute the free-divergence condition for Maxwell equations ($\nabla \cdot E = 0$). To consider this point, we computed, for different meshes of the same example of cavity and different orders of approximation, an equivalent H^{-1} norm of the divergence of the electric discrete fields E_h, proposed by Cockburn et al. [25]:

$$\|\mathbf{E}_h\|_{*,h} = \sum_{\Gamma \in \mathbf{F}} \int_{\Gamma}^{G} |[\![\mathbf{E}_h \cdot \mathbf{n}]\!]| + \sum_{\Gamma \in \mathscr{T}_h} \int_{K}^{G} |\nabla \cdot \mathbf{E}_h|.$$

Figs. 3 and 4 show the results obtained by using different sizes of cells in the mesh and different orders of approximation, respectively. These results confirm the interest in using high spatial approximation order despite order 2 in time.

In the previous results, the error is principally due to the dispersive phenomena, since it can be easily be proven that our numerical scheme, with a leap-frog scheme in time, remains conservative. The energetic quantity taken into account for this proof is given by

$$\sum_{K \in \mathscr{T}_h} \int_K \varepsilon \mathbf{E}_K^n \cdot \mathbf{E}_K^n \, \mathrm{d}K + \int_K \mu_0 \mathbf{H}_K^{n+\frac{1}{2}} \cdot \mathbf{H}_K^{n-\frac{1}{2}} \, \mathrm{d}K,$$

where $(\mathbf{E}_K^n, \mathbf{H}_K^n)$ are electric and magnetic fields values taken on K at time t_n (see [26]).

Table 2
Numerical dispersion and dissipation orders by using non-centered fluxes

Order of approximation	$r = 1$	$r = 2$	$r = 3$	$r = 4$	$r = 5$
Order of dispersive error	4	6	8	10	12
Order of dissipative error	3	5	7	9	11

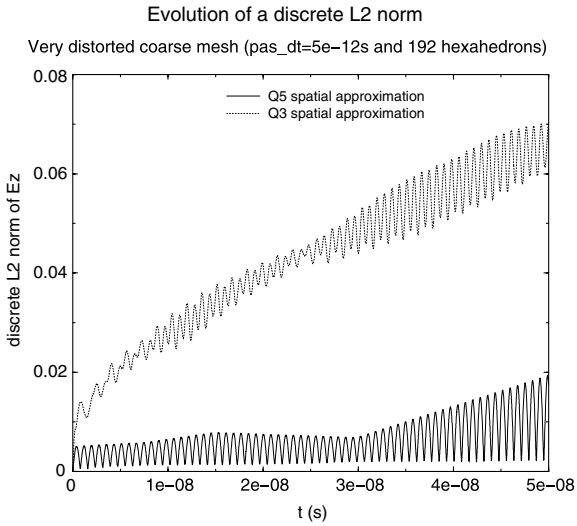

Fig. 2. Evolution of the L^2 error in time for spatial order equal to 3 and 5.

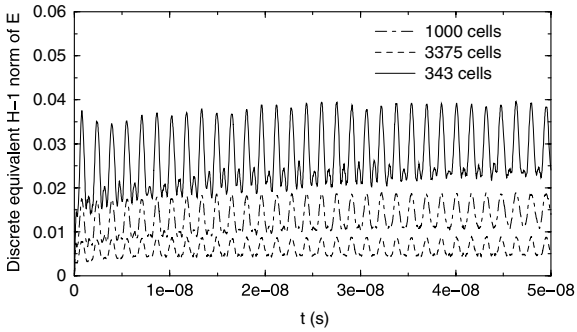

Fig. 3. h-Convergence by using a Q_3 order.

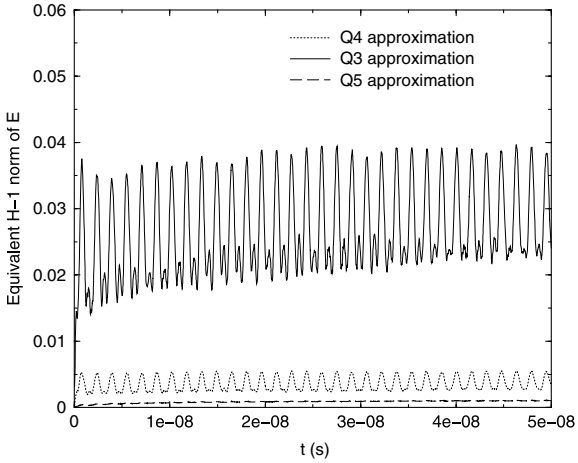

Fig. 4. p-Convergence by using mesh constituted of 343 cells.

Now, we are interested in the stability of the fully discrete scheme. In a first step, we study the stability by a plane wave technique on a homogeneous infinite grid. This technique provides necessary and sufficient stability conditions of the scheme on a regular mesh. In a second step, we use an energy technique to prove the stability on non-structured hexahedral meshes. We get a sufficient stability condition. Moreover, we show that our scheme conserves a discrete energy. This property confirms the non-dissipative nature of the scheme.

3.2.7.1. CFL conditions obtained by a plane waves technique. For a Cartesian homogeneous grid, we proceed as for the spatial dispersion analysis except that we add the time discretization. Then, the numerical plane wave becomes:

$$\begin{aligned}(E^n_{i,j,k,\mathbf{p}})^l &= E^l_{ijk}\mathrm{e}^{\mathrm{i}(\omega_h n\Delta t - k_1 hp_1 - k_2 hp_2 - k_3 hp_3)}\mathrm{e}^{-\mathrm{i}(\hat{x}_i k_1 h + \hat{y}_j k_2 h + \hat{z}_k k_3 h)},\\ (H^{n-\frac{1}{2}}_{ijk,\mathbf{p}})^l &= H^l_{ijk}\mathrm{e}^{\mathrm{i}(\omega_h\left(n-\frac{1}{2}\right)\Delta t - k_1 hp_1 - k_2 hp_2 - k_3 hp_3)}\mathrm{e}^{-\mathrm{i}(\hat{x}_i k_1 h + \hat{y}_j k_2 h + \hat{z}_k k_3 h)}.\end{aligned} \tag{24}$$

So, spectral problem (22) is rewritten $\forall l = 1,\ldots,3$:

$$\begin{aligned}\frac{4h^2}{c^2\Delta t^2}\sin\left(\frac{\omega_h\Delta t}{2}\right)E^l &= \alpha E^l,\\ \frac{4h^2}{c^2\Delta t^2}\sin\left(\frac{\omega_h\Delta t}{2}\right)H^l &= \alpha H^l.\end{aligned} \tag{25}$$

So, we deduce the space-time dispersion relations:

$$\sin^2\left(\frac{\omega_h\Delta t}{2}\right) = \frac{\Delta t^2 c^2}{4h^2}\left(\omega_h[k_1]^2 + \omega_h[k_2]^2 + \omega_h[k_3]^2\right), \tag{26}$$

where $\omega_h[k_i]^2$ is defined as in Theorem 1.

Finally, the numerical scheme is stable if and only if

$$\frac{\Delta t}{h} \leqslant \frac{2}{c}\frac{1}{\max\left(\sqrt{\omega_h[k_1]^2 + \omega_h[k_2]^2 + \omega_h[k_3]^2}\right)} = \frac{c_r}{\sqrt{3}}, \tag{27}$$

where the max is taken on all the eigenvalues of the 1D problem for $i = 1,2,3$ and c_r corresponds to CFL number for the same 1D scheme using an order r of polynomial approximation.

The values of c_r can be numerically determined and for $r = 1$, 2, 3, 4 and 5 we obtain 0.5, 0.247, 0.15, 0.101 and 0.0732, respectively.

It is thus sufficient to divide by $\sqrt{3}$ to obtain 3D CFL conditions.

3.2.7.2. Stability by energy technique. To prove the stability of the DG scheme by an energy technique, we use the same approach as the one used by Piperno et al. in [26] on a non-dissipative finite volume scheme.

The discrete energy, which naturally appears when one uses a leapfrog scheme for the time domain approximation, is defined by

$$\mathscr{E}^n_h = \sum_{K\in\mathscr{T}_h}\mathscr{E}^n_K, \tag{28}$$

where $\forall K \in \mathscr{T}_h$,

$$\mathscr{E}^n_K = \int_K^G \varepsilon_K \mathbf{E}^n_{hK}\cdot\mathbf{E}^n_{hK}\,\mathrm{d}x + \int_K^G \mu_K \mathbf{H}^{n+\frac{1}{2}}_{hK}\cdot\mathbf{H}^{n-\frac{1}{2}}_{hK}\,\mathrm{d}x. \tag{29}$$

We easily show that this energy is conserved during the discrete time, i.e., $\forall n \geqslant 0$, we have

$$\mathscr{E}^{n+1}_h - \mathscr{E}^n_h = 0, \tag{30}$$

and that it can only be expressed as a function of the variables $\tilde{\mathbf{E}}^n_h$ and $\tilde{\mathbf{H}}^{n+\frac{1}{2}}_h$:

$$\mathscr{E}_h^n = \sum_{K\in\mathscr{T}_h}\left[\int_K^G \tilde{\mathbf{E}}_{hK}^n\cdot\tilde{\mathbf{E}}_{hK}^n\,\mathrm{d}x + \int_K^G \tilde{\mathbf{H}}_{hK}^{n+\frac{1}{2}}\cdot\tilde{\mathbf{H}}_{hK}^{n+\frac{1}{2}}\,\mathrm{d}x + \frac{\Delta t}{2\sqrt{\varepsilon_K\mu_K}}\int_K^G \nabla\times\tilde{\mathbf{E}}_{hK}^n\cdot\tilde{\mathbf{H}}_{hK}^{n+\frac{1}{2}}\,\mathrm{d}x \right.$$
$$+\frac{\Delta t}{2\sqrt{\varepsilon_K\mu_K}}\int_K^G \tilde{\mathbf{E}}_{hK}^n\cdot\nabla\times\tilde{\mathbf{H}}_{hK}^{n+\frac{1}{2}}\,\mathrm{d}x - \frac{\Delta t}{2\sqrt{\varepsilon_K\mu_K}}\sum_{i=1}^{\mathrm{nbfi}_K}\int_{\Gamma_{\rho(i,K)}}^G(\tilde{\mathbf{E}}_{hV(i,K)}^n\times\mathbf{n}_K)\cdot\tilde{\mathbf{H}}_{hK}^{n+\frac{1}{2}}\,\mathrm{d}\sigma_{\rho(i,K)}$$
$$\left.+\frac{\Delta t}{2\sqrt{\varepsilon_K\mu_K}}\sum_{i=1}^{6}\int_{\Gamma_{\rho(i,K)}}^G(\tilde{\mathbf{E}}_{hK}^n\times\mathbf{n}_K)\cdot\tilde{\mathbf{H}}_{hK}^{n+\frac{1}{2}}\,\mathrm{d}\sigma_{\rho(i,K)}\right], \tag{31}$$

where $\tilde{\mathbf{E}}_{hK}^n = \mathbf{E}_{hK}^n\sqrt{\varepsilon_K}$, $\tilde{\mathbf{H}}_{hK}^{n+\frac{1}{2}} = \mathbf{H}_{hK}^{n+\frac{1}{2}}\sqrt{\mu_K}$, $V(i,K)$ is the neighbor of K containing the face $\Gamma_{\rho(i,K)}$ and nbfi_K is the number of faces of K belonging to $\mathscr{F}_h^i$.

From now, we can eliminate the exponent in n and the tildes in the notation, since we study the quadratic form (31) for all the variables $\mathbf{E}_h$, $\mathbf{H}_h$. To prove the L^2-stability, it would suffices if we determine a condition for which this quadratic form is definite positive. In this case, $\mathscr{E}_h^n$ will define a norm.

Proposition 2. *We have the estimate*

$$\mathscr{E}_h \geqslant \hat{\mathscr{E}}_h, \tag{32}$$

where

$$\hat{\mathscr{E}}_h = \sum_{K\in\mathscr{T}_h}\left[\Lambda_K\int_{\hat{K}}^G\hat{\mathbf{E}}_K\cdot\hat{\mathbf{E}}_K\,\mathrm{d}\hat{x} + \Lambda_K\int_{\hat{K}}^G\hat{\mathbf{H}}_K\cdot\hat{\mathbf{H}}_K\,\mathrm{d}\hat{x} + \frac{\Delta t}{2\sqrt{\varepsilon_K\mu_K}}\mathrm{sign}(J_K)\int_{\hat{K}}^G\hat{\nabla}\times\hat{\mathbf{E}}_K\cdot\hat{\mathbf{H}}_K\,\mathrm{d}\hat{x}\right.$$
$$+\frac{\Delta t}{2\sqrt{\varepsilon_K\mu_K}}\mathrm{sign}(J_K)\int_{\hat{K}}^G\hat{\mathbf{E}}_K\cdot\hat{\nabla}\times\hat{\mathbf{H}}_K\,\mathrm{d}\hat{x} + \sum_{i=1}^{\mathrm{nbfi}_K}\frac{\Delta t}{2\sqrt{\varepsilon_{V(i,K)}\mu_K}}\mathrm{sign}(J_{V(i,K)})$$
$$\left.\times\int_{\hat{\Gamma}_{i'}}^G(\hat{\mathbf{E}}_{V(i,K)}\times\hat{\mathbf{n}}_{i'})\cdot N_{V(i,K)\to K}^*\hat{\mathbf{H}}_K o\mathscr{G}_{V(i,K)\to K}\,\mathrm{d}\hat{\sigma}_{i'} + \frac{\Delta t}{2\sqrt{\varepsilon_K\mu_K}}\sum_{i=\mathrm{nbfi}_K+1}^{6}\mathrm{sign}(J_K)\int_{\hat{\Gamma}_i}^G(\hat{\mathbf{E}}_K\times\hat{\mathbf{n}}_i)\cdot\hat{\mathbf{H}}_K\,\mathrm{d}\hat{\sigma}_i\right] \tag{33}$$

and

$$\Lambda_K = \min_{1\leqslant i,j,k\leqslant r+1}\left(\frac{|J_K(\hat{x}_i,\hat{y}_j,\hat{z}_k)|}{\lambda_{\max}((DF_K^*DF_K)(\hat{x}_i,\hat{y}_j,\hat{z}_k))}\right) \tag{34}$$

with $\lambda_{\max}(DF_K^*DF_K)$ the greatest eigenvalue of $DF_K^*DF_K$.

Proof. To show Λ_k, it would suffices if we to use the expression of the mass terms and take the minimum of these terms on the Gauss points. Then, we use the properties of stiffness and jump matrices previously, which were presented to prove the result. □

Let $\hat{\mathscr{R}}$, $\hat{\mathscr{D}}$ and $\hat{\mathscr{B}}$ be the $3(r+1)^3\times 3(r+1)^3$ matrices defined by: $\forall i,i'\in\{1,2,3\}$ and $\forall\mathbf{l},\mathbf{l}'\in\{1,\ldots,r+1\}^3$

$$\begin{aligned}
\hat{\mathscr{R}}((i,\mathbf{l}),(i',\mathbf{l}')) &= \int_{\hat{K}}\hat{\nabla}\times\hat{\boldsymbol{\varphi}}_{\mathbf{l}}^i\cdot\hat{\nabla}\times\hat{\boldsymbol{\varphi}}_{\mathbf{l}'}^{i'}\,\mathrm{d}\hat{\mathbf{x}},\\
\hat{\mathscr{D}}((i,\mathbf{l}),(i',\mathbf{l}')) &= \delta_{ii'}\delta_{\mathbf{l}\mathbf{l}'}\hat{\omega}_{\mathbf{l}},\\
\hat{\mathscr{B}}((i,\mathbf{l}),(i',\mathbf{l}')) &= \int_{\partial\hat{K}}(\hat{\boldsymbol{\varphi}}_{\mathbf{l}}^i\times\hat{\mathbf{n}})\cdot(\hat{\boldsymbol{\varphi}}_{\mathbf{l}'}^{i'}\times\hat{\mathbf{n}})\,\mathrm{d}\hat{\sigma}.
\end{aligned} \tag{35}$$

We are now going to estimate the terms of (33) in the function of $\|\hat{\mathbf{E}}_K\|_{0,\hat{K}}$ and $\|\hat{\mathbf{H}}_K\|_{0,\hat{K}}$ and to prove the L^2-stability:

Theorem 2. *The condition given by*

$$\frac{\Delta t}{\Lambda_K} < \frac{2}{c_K}\frac{1}{\sqrt{\lambda_{\max}\left(\hat{\mathscr{D}}^{-\frac{1}{2}}\hat{\mathscr{R}}\hat{\mathscr{D}}^{-\frac{1}{2}}\right)} + \frac{1}{2}\max\limits_{1\leqslant i\leqslant\mathrm{nbfi}_K}\left(\sqrt{\frac{\mu_K}{\mu_{V(i,K)}}},\sqrt{\frac{\varepsilon_K}{\varepsilon_{V(i,K)}}}\right)\lambda_{\max}\left(\hat{\mathscr{D}}^{-\frac{1}{2}}\hat{\mathscr{B}}\hat{\mathscr{D}}^{-\frac{1}{2}}\right)}, \tag{36}$$

$\forall K\in\mathscr{T}_h$, *is sufficient to ensure the stability of the DG scheme, where* $c_K = \frac{1}{\sqrt{\varepsilon_K\mu_K}}$

Proof. We have

$$\int_{\hat{K}}^{G} \hat{\nabla} \times \hat{\mathbf{E}}_K \cdot \hat{\mathbf{H}}_K \, \mathrm{d}\hat{x} \leqslant \|\hat{\nabla} \times \hat{\mathbf{E}}_K\|_{0,\hat{K}} \|\hat{\mathbf{H}}_K\|_{0,\hat{K}}. \tag{37}$$

Using the matrices defined in (35), we easily see that:

$$\int_{\hat{K}}^{G} \hat{\nabla} \times \hat{\mathbf{E}}_K \cdot \hat{\mathbf{H}}_K \, \mathrm{d}\hat{x} \leqslant \sqrt{\lambda_{\max}\left(\hat{\mathscr{D}}^{-\frac{1}{2}} \hat{\mathscr{R}} \hat{\mathscr{D}}^{-\frac{1}{2}}\right)} \|\hat{\mathbf{E}}_K\|_{0,\hat{K}} \|\hat{\mathbf{H}}_K\|_{0,\hat{K}}. \tag{38}$$

Now we estimate the surface terms:

$$\begin{aligned}
&\frac{1}{\sqrt{\varepsilon_{V(i,K)}\mu_K}} \int_{\hat{\Gamma}_{i'}}^{G} (\hat{\mathbf{E}}_{V(i,K)} \times \hat{\mathbf{n}}_{i'}) \cdot N^*_{V(i,K)\to K} \hat{\mathbf{H}}_K o \mathscr{G}_{V(i,K)\to K} \, \mathrm{d}\hat{\sigma}_{i'} \\
&\quad \leqslant \frac{1}{\sqrt{\varepsilon_{V(i,K)}\mu_K}} \|(\hat{\mathbf{E}}_{V(i,K)} \times \hat{\mathbf{n}}_{i'})\|_{0,\hat{\Gamma}_{i'}} \|(\hat{\mathbf{n}}_{i'} \times (N^*_{V(i,K)\to K} \hat{\mathbf{H}}_K o \mathscr{G}_{V(i,K)\to K} \times \hat{\mathbf{n}}_{i'}))\|_{0,\hat{\Gamma}_{i'}} \\
&\quad \leqslant \frac{1}{\sqrt{\varepsilon_{V(i,K)}\mu_K}} \|(\hat{\mathbf{E}}_{V(i,K)} \times \hat{\mathbf{n}}_{i'})\|_{0,\hat{\Gamma}_{i'}} \|(\hat{\mathbf{H}}_K \times \hat{\mathbf{n}}_i)\|_{0,\hat{\Gamma}_i} \\
&\quad \leqslant \frac{1}{2}\left[c_{V(i,K)} \sqrt{\frac{\mu_{V(i,K)}}{\mu_K}} \|(\hat{\mathbf{E}}_{V(i,K)} \times \hat{\mathbf{n}}_{i'})\|^2_{0,\hat{\Gamma}_{i'}} + c_K \sqrt{\frac{\varepsilon_K}{\varepsilon_{V(i,K)}}} \|(\hat{\mathbf{H}}_K \times \hat{\mathbf{n}}_i)\|^2_{0,\hat{\Gamma}_i} \right],
\end{aligned} \tag{39}$$

where $c_K = \frac{1}{\sqrt{\varepsilon_K \mu_K}}$.

In the same way, we obtain:

$$\int_{\hat{\Gamma}_i}^{G} (\hat{\mathbf{E}}_K \times \hat{\mathbf{n}}_i) \cdot \hat{\mathbf{H}}_K \, \mathrm{d}\hat{\sigma}_i \leqslant \frac{1}{2}\left[\|(\hat{\mathbf{E}}_K \times \hat{\mathbf{n}}_i)\|^2_{0,\hat{\Gamma}_i} + \|(\hat{\mathbf{H}}_K \times \hat{\mathbf{n}}_i)\|^2_{0,\hat{\Gamma}_i} \right]. \tag{40}$$

Finally, we have

$$\begin{aligned}
&\sum_{K\in\mathscr{T}_h} \left[-\sum_{i=1}^{\mathrm{nbfi}_K} \frac{1}{\sqrt{\varepsilon_{V(i,K)}\mu_K}} \mathrm{sign}(J_{V(i,K)}) \int_{\hat{\Gamma}_{i'}}^{G} (\hat{\mathbf{E}}_{V(i,K)} \times \hat{\mathbf{n}}_{i'}) \cdot N^*_{V(i,K)\to K} \hat{\mathbf{H}}_K o \mathscr{G}_{V(i,K)\to K} \, \mathrm{d}\hat{\sigma}_{i'} \right. \\
&\qquad \left. + \frac{1}{\sqrt{\varepsilon_K \mu_K}} \sum_{i=\mathrm{nbfi}_K+1}^{6} \mathrm{sign}(J_K) \int_{\hat{\Gamma}_i}^{G} (\hat{\mathbf{E}}_K \times \hat{\mathbf{n}}_i) \cdot \hat{\mathbf{H}}_K \, \mathrm{d}\hat{\sigma}_i \right] \\
&\qquad \leqslant \frac{1}{2} \sum_{K\in\mathscr{T}_h} c_K \max_{1\leqslant i\leqslant \mathrm{nbfi}_K} \left(\sqrt{\frac{\mu_K}{\mu_{V(i,K)}}}, \sqrt{\frac{\varepsilon_K}{\varepsilon_{V(i,K)}}} \right) \left[\|(\hat{\mathbf{E}}_K \times \hat{\mathbf{n}})\|^2_{0,\partial\hat{K}} + \|(\hat{\mathbf{H}}_K \times \hat{\mathbf{n}})\|^2_{0,\partial\hat{K}} \right] \\
&\qquad \leqslant \frac{\lambda_{\max}\left(\hat{\mathscr{D}}^{-\frac{1}{2}} \hat{\mathscr{B}} \hat{\mathscr{D}}^{-\frac{1}{2}}\right)}{2} \sum_{K\in\mathscr{T}_h} c_K \max_{1\leqslant i\leqslant \mathrm{nbfi}_K} \left(\sqrt{\frac{\mu_K}{\mu_{V(i,K)}}}, \sqrt{\frac{\varepsilon_K}{\varepsilon_{V(i,K)}}} \right) \left[\|\hat{\mathbf{E}}_K\|^2_{0,\hat{K}} + \|\hat{\mathbf{H}}_K\|^2_{0,\hat{K}} \right].
\end{aligned} \tag{41}$$

Eqs. (38) and (41) then lead to

$$\begin{aligned}
\hat{\mathscr{E}}_h \geqslant \sum_{K\in\mathscr{T}_h} \Lambda_K \Bigg[&\left(1 - \frac{\Delta t c_K}{4\Lambda_K} \max_{1\leqslant i\leqslant \mathrm{nbfi}_K} \left(\sqrt{\frac{\mu_K}{\mu_{V(i,K)}}}, \sqrt{\frac{\varepsilon_K}{\varepsilon_{V(i,K)}}} \right) \lambda_{\max}\left(\hat{\mathscr{D}}^{-\frac{1}{2}} \hat{\mathscr{B}} \hat{\mathscr{D}}^{-\frac{1}{2}}\right) \right) \|\hat{\mathbf{E}}_K\|^2_{0,\hat{K}} \\
&+ \left(1 - \frac{\Delta t c_K}{4\Lambda_K} \max_{1\leqslant i\leqslant \mathrm{nbfi}_K} \left(\sqrt{\frac{\mu_K}{\mu_{V(i,K)}}}, \sqrt{\frac{\varepsilon_K}{\varepsilon_{V(i,K)}}} \right) \lambda_{\max}\left(\hat{\mathscr{D}}^{-\frac{1}{2}} \hat{\mathscr{B}} \hat{\mathscr{D}}^{-\frac{1}{2}}\right) \right) \|\hat{\mathbf{H}}_K\|^2_{0,\hat{K}} \\
&- \frac{\Delta t c_K}{\Lambda_K} \sqrt{\lambda_{\max}\left(\hat{\mathscr{D}}^{-\frac{1}{2}} \hat{\mathscr{R}} \hat{\mathscr{D}}^{-\frac{1}{2}}\right)} \|\hat{\mathbf{E}}_K\|_{0,\hat{K}} \|\hat{\mathbf{H}}_K\|_{0,\hat{K}} \Bigg],
\end{aligned} \tag{42}$$

which ends the proof of the theorem. □

4. Numerical results

To validate and to illustrate the advantages of this method, several comparisons on simple scattering problems with different other methods are made. In these comparisons, we are interested in the fields near the structure (EMC problems) or by far fields (RCS) for scattering objects and by the fields inside cavities. The methods used to compare the results with our method are finite difference time domain (FDTD) [1], finite volume time domain (FVTD) [24] and marching on time (MOT) [4] methods.

4.1. Near fields and far fields for curved objects

The first example consists in evaluating the field scattered by a perfectly plate cone, at two test-points A and B located near the structure. Fig. 5 shows the location of the test-points around the object. The cone is illuminated with a plane wave given by $f(t) = E_y e^{-\gamma^2}$, with $\gamma = 3e8t - z + 6$. The incidence is along the axis z and the minimum wavelength is approximately 300 MHz.

Fig. 6 shows a comparison between the solutions obtained with the different methods.

In this comparison, to obtain an accurate result for the FDTD method, it is necessary to use a mesh with a spatial step size smaller than $0.025m = \lambda/40$. The classical $\lambda/10$ criterion is not sufficient to obtain a correct solution in this case.

The need to use a very small spatial step size implies a small time step (4.e−11 s) and a more important number of cells in the computational domain (596,232), which dramatically increases the memory storage (27 Mo) and the CPU time consumed in the FDTD method (99 min on a Pentium 4 at 3 GHz). In these conditions, the discontinuous Galerkin approach is more interesting (25 min with a Q_3-approximation for 15 Mo of memory storage).

For the FVTD method, the results obtained with a spatial averaged step size equal to $\lambda/10$ are correct due to the fact of taking accurately into account the shape of the object with a reasonable number of cells in the domain (46,292), which implies a low memory storage (6 Mo). But the apparition of little cells in the unstructured mesh induces a little time step (2.e−7 s) to guarantee the stability and a supplementary cost in the CPU time for the FVTD solution (35 min). In this condition, the discontinuous Galerkin method again remains more interesting in terms of CPU time.

The second example consists in evaluating the backscattered far field of a perfectly metallic sphere of radius 1 m. Fig. 7 shows a comparison of the solutions obtained by the discontinuous Galerkin approach, the FDTD method and a time domain EFIE method (MOT), which is considered to be the reference solution. We can see

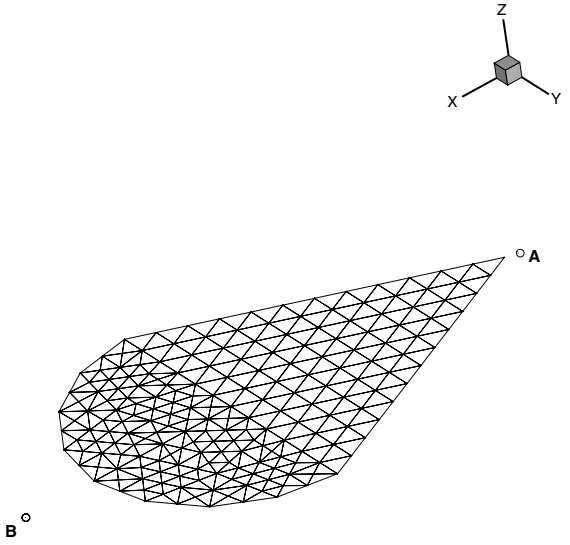

Fig. 5. Location of the test-points on the cone.

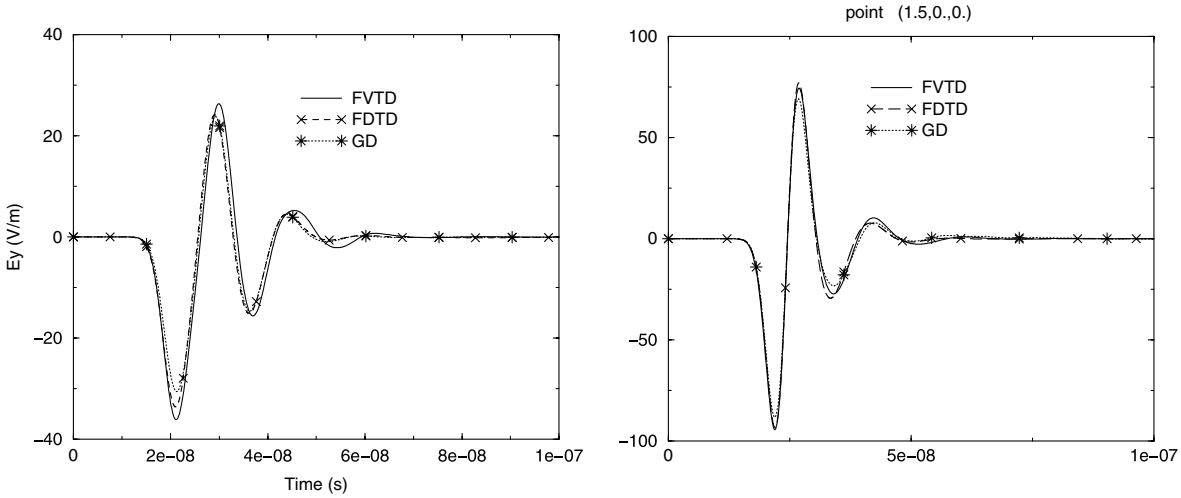

Fig. 6. Comparisons of the solutions obtained with different methods at the test-points A and B.

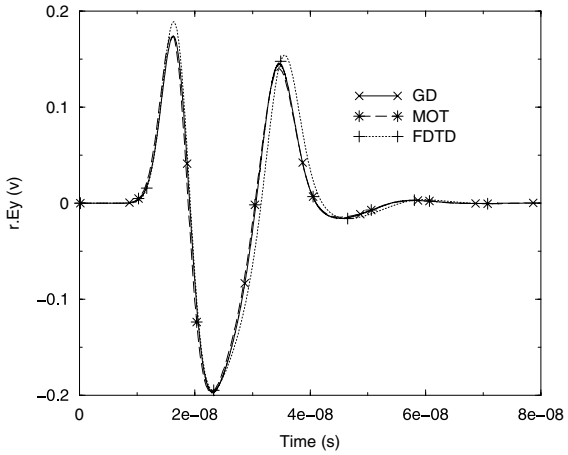

Fig. 7. Backscattered far fields obtained with different methods. The point is located at $r = 100$ m of the center of the sphere.

the perfect agreement between the DG and MOT solutions and the difficulty to coincide with the FDTD method. This is probably due to the staircase approach of the semi-disk. Again, in this example, the GDM allows us to obtain an accurate solution with the same advantage of memory and CPU time as for the previous example.

In these methods, the far fields are computed by an integral formula using electric and magnetic currents taken on a fictitious surface which encloses the scattered object [30].

4.2. Cavity problems and behavior of the solution at long time

For cavities or for long time experiments, the dispersion and the dissipation errors of the numerical scheme play a very important role. In these kinds of problems, the high order character of the method is crucial to obtain an accurate solution. To illustrate this purpose, we first study the propagation of a mode inside a perfectly metallic cubic cavity ($\mathbf{E} \times \mathbf{n} = 0$ on the wall of the cavity) with an edge of $1m$. The propagative mode studied is a mode $(m, n, 0)$ given by

$$\begin{cases} E_x = 0; \quad E_y = 0; \quad H_z = 0, \\ E_z = \sin(m\pi x)\sin(n\pi y)\cos(\omega t), \\ H_x = \frac{1}{\omega\mu_0}\pi n \sin(m\pi x)\cos(n\pi y)\sin(\omega t), \\ H_y = \frac{1}{\omega\mu_0}\pi m \cos(m\pi x)\sin(n\pi y)\sin(\omega t). \end{cases} \tag{43}$$

Fig. 8 shows the comparison between the exact and the computed solutions for a given mode ($m = n = 3$) inside the cavity by using different orders of approximation and different mesh sizes. The advantage of using high order schemes in this kind of problem appears clearly. We also notice the reduction of the number of cells needed to get an accurate solution when the order increases. This also induces a gain of CPU time. Fig. 9 shows a comparison between computed solutions obtained on different meshes with the FDTD and the discontinuous Galerkin (Q_5-approximation) methods. We notice on this example the good behavior of the discontinuous Galerkin method after 180 wavelengths.

The next example is the evaluation of scattered fields for a long time of observation. Generally, for perfectly metallic objects with dimension of a few wavelengths (<10), the time of observation of the scattered signals is short. This is not the case for dielectric objects or for large objects (>100 wavelengths). So it is worth perform-

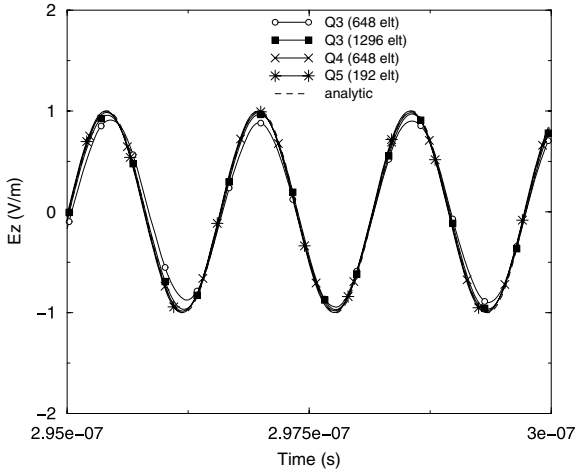

Fig. 8. Electric field taken inside a cavity after 180 wavelengths.

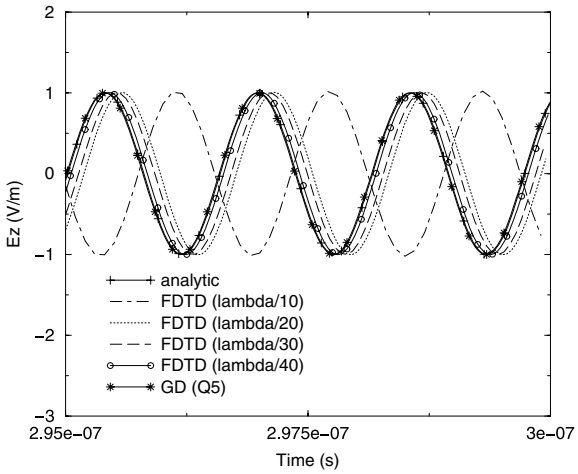

Fig. 9. Comparison FDTD and discontinuous Galerkin methods inside a cavity.

ing this kind of experiment with our method. The configuration proposed is defined by a metallic sphere of internal radius equal to 50 cm coated with a layer (thickness: 25 cm) of a dielectric material ($\varepsilon_r = 10$). This object is illuminated by a plane wave defined by ($k_x = 1$, $E_y = 377f(t,x)$, $H_z = f(t,x)$) with $f(t,x) = \exp(-(5e8(t-(x+20/3e8))^2))$ and we evaluate the field at a test-point A located at 1 cm of the object (see Fig. 10).

The presence of the dielectric material makes the solution be unsteady for long observation time. In Fig. 11, one can see the behavior of the solutions of the problems obtained by FDTD and ours for different sizes of cells and different orders of approximation.

We can see in these figures the advantage of having a high order method to obtain a solution avoiding dispersion error. In the results shown in the previous figures, we use for FDTD ($\lambda/20$) a mesh of 6,751,269 cells (309 Mo) compared to 16,984 cells (42 Mo) for a Galerkin discontinuous Q_3-approximation (we use the same number of cells for the Q_5-approximation (192 Mo) with a quite similar solution as for Q_3-approximation). The CPU times are similar between FDTD ($\lambda/40$) and the Q_3-approximation, but at long time of observation, the solutions are very different. To improve the FDTD solution, we need to use a smaller spatial step and in this case, the values of CPU time and memory storage obtained clearly show the efficiency of our method in such experiments.

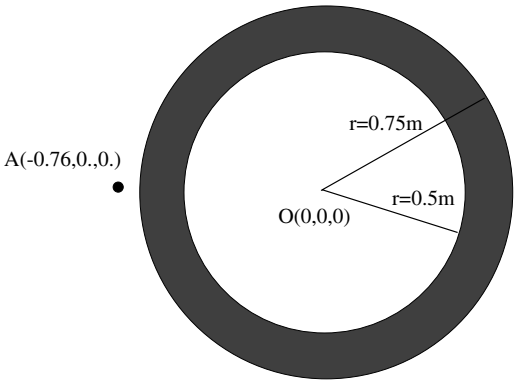

Fig. 10. Cut of the object at the plane $z = 0$.

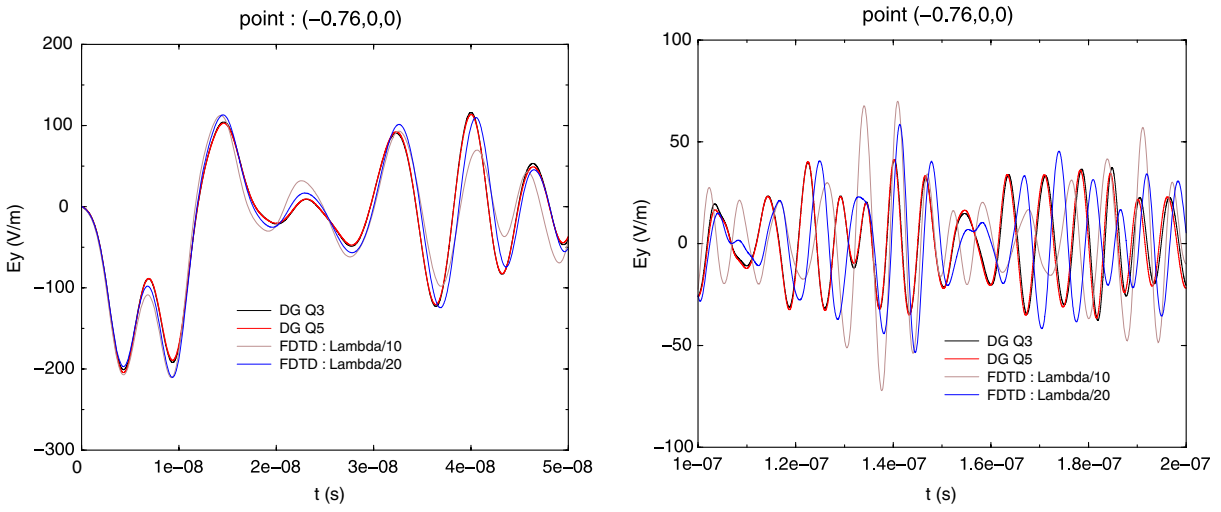

Fig. 11. Evolution of the fields at observation times corresponding to 20 wavelengths and to 80 wavelengths.

5. Local time-stepping strategy

All these examples clearly prove the capacity of our method to take into account curved geometries and to decrease the dispersion error in cavity problems or at long times. Of course, the efficiency of the method lies in the possibility to get high order spatial approximation with reasonable memory storage and CPU time. However, the difficulty of this approach consists in obtaining a mesh only based on hexahedral cells. An efficient method consists in constructing an initial mesh composed of tetrahedral cells and then, in splitting each cell into four hexahedral cells. The drawback of this method is the very distorted character of the final mesh and the fact that the size of some cells can be very little (as in tetrahedral meshes). Moreover, we have noticed some problems of stability at high order in the classical PML [29], on some examples by using very distorted meshes. To avoid this problem, another approach consists in using, for instance, an absorbing boundary condition strategy [31]. However, generally, this approach needs to have the boundary of the computational domain far from the object in order to get reasonable reflections. This condition can increase the computational domain and the CPU time.

For all these reasons, the use of a local time-stepping strategy seems to be interesting.

The local time-stepping strategy that we propose has been applied to some scattering problems and gives very good results for our actual experiments where the largest time of observation is on 100 wavelengths.

5.1. Proposed strategy

We can write our discontinuous Galerkin method as

$$\begin{cases} H^{n+\frac{1}{2}} - H^{n-\frac{1}{2}} = \mathrm{d}t\, f_E(E^n), \\ E^{n+1} - E^n = \mathrm{d}t\, f_H(H^{n+\frac{1}{2}}), \end{cases} \tag{44}$$

where E, H are the electric and magnetic fields, respectively, and f_E, f_H are linear functions. $\mathrm{d}t$ defines the time step verifying the stability condition:

$$\mathrm{d}t < cfl \frac{\mathrm{d}l}{v} \tag{45}$$

where v is the velocity of light in the medium, $\mathrm{d}l$ the size of the cell and cfl a strict positive number.

When the condition (45) is applied to each cell of the mesh, the value of $\mathrm{d}t$ varies from cell to cell. To ensure the stability, the minimum value $\mathrm{d}t_{\min} = \min \mathrm{d}t$ is taken as the time-step of the method. In our strategy, we propose to define a value $\mathrm{d}t_c = 2(n+1)\mathrm{d}t_{\min}$, where n is a given integer and take this value as the time step of the method. Then, to ensure the stability condition, we obtain two sets of cells where the fields in the first one labelled 1 are computed by using a time step equal to $\mathrm{d}t_{\min}$ (the values of $\mathrm{d}t$ of each cell in this set are smaller than $\mathrm{d}t_c$) and a second, labelled 2, where the fields are computed by using a time step equal to $\mathrm{d}t_c$.

In the time process, we obtain for one step in the set of cells labelled 2, $2(n+1)$ local steps in the set of cells labelled 1. To compute the fields located in the two sets, we need some values of fields located in the other set. The difficulty of the local time-stepping process is to have the fields at the appropriate time in each step. This is generally obtained by doing interpolations, but this is more difficult in the leap-frog scheme presented above.

The strategy proposed to obtained this coincidence of time is the following:

- mark with number 3 the cells labelled 2 which are neighbors of the cells labelled 1;
- mark with number 4 the cells labelled 2 which are neighbors of the cells labelled 3. At this step, we obtain a configuration of labelled cells as represented in Fig. 12.
- assume we know the magnetic and electric fields in the computational domain, respectively, for the time $(m-\frac{1}{2})\mathrm{d}t_c$ and $t_m = m\,\mathrm{d}t_c$. At each step $\mathrm{d}t_c$, we have the following sequence:
  - save at the time $t_m - \frac{\mathrm{d}t_c}{2}$ in H_s the H fields and at the time t_m in E_s the electric fields for the cells marked 3 and 4;
  - compute H for all the cells marked 2,3 and 4 at the time $t_m + \frac{\mathrm{d}t_c}{2}$;
  - put $t_0 = t_m$;

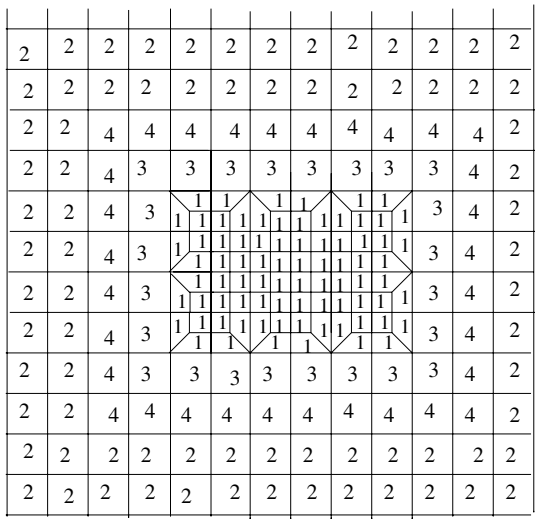

Fig. 12. Example of local time step cell marking.

- for each local step 1 to n
  - compute H for all cells marked 1 at the time $t_0 + \frac{\mathrm{d}t_{\min}}{2}$;
  - interpolate H for the cells marked 3 and 4 at the time $t_0 + \frac{\mathrm{d}t_{\min}}{2}$ by using H_s fields and the H fields previously evaluated at the time $t_m + \frac{\mathrm{d}t_c}{2}$;
  - compute E for the cells marked 1 and 3 at the time $t_0 + \mathrm{d}t_{\min}$;
  - increase $t_0 = t_0 + \mathrm{d}t_{\min}$;
- evaluate the H fields in cells marked 1 at the time $t_0 + \frac{\mathrm{d}t_{\min}}{2}$, which is equal to $t_m + \frac{\mathrm{d}t_c}{2}$ by the choice made on $\mathrm{d}t_c$;
- restore E_s values in E for the cells marked 3 and 4;
- save at the time t_m, the electric fields of the cells marked 3 and 4 in E_s and the magnetic fields H at the time of the cells marked 3 and 4 in H_s;
- evaluate the electric fields E for the cells marked 2,3 and 4 at the time $t_m + \mathrm{d}t_c$;
- put $t_0 = t_m + \frac{\mathrm{d}t_c}{2}$;
- for each local step 1 to n
  - evaluate the electric fields E for the cells marked 1 at the time $t_0 + \frac{\mathrm{d}t_{\min}}{2}$;
  - interpolate the electric fields E for the cells marked 3 and 4 at the time $t_0 + \frac{\mathrm{d}t_{\min}}{2}$ with the values E_s and E previously computed at the time $t_m + \mathrm{d}t_c$;
  - evaluate the magnetic fields H for the cells marked 1 and 3 at the time $t_0 + \mathrm{d}t_{\min}$;
  - increase $t_0 = t_0 + \mathrm{d}t_{\min}$;
- evaluate the electric fields E for the cells marked 1 at the time $t_0 + \frac{\mathrm{d}t_{\min}}{2}$;
- restore the H_s values in H for the cells marked 3 and 4;
- increase $t_m = t_m + \mathrm{d}t_c$;

The strategy presented here has two different time steps, but it is also possible to have more of them. In this case, we only need to mark more cells with different numbers. For our applications, we do not use more local time steps because the most important point is to eliminate the very small cells in order to have a time step for the process large enough.

5.2. Numerical examples

To show the interest of this strategy, we consider a plane wave illuminating a cone, as previously studied in the numerical results section. The scattered fields are observed at the test-point A (see Fig. 5).

To obtain the unstructured mesh of the computational domain, we enclose the cone inside a sphere where an absorbing condition of order 1 is applied (condition of Silver-Muller). The domain between the cone and the sphere is given by a set of tetrahedric cells, which are split into four hexaehdric cells. This kind of mesh implies that the size of a lot of cells cannot be easily controlled. Consequently, the obtained mesh contains cells with large variation of size. Therefore, it is interesting to apply in this case a local time-stepping strategy in our method.

Fig. 13 shows a part of the unstructured mesh where we can see the significant difference between the size of the cells. In particular, in this mesh, the smallest size of the cell is equal to 0.02 m, the largest size to 0.45 m and the averaged size to 0.2 m . In our Galerkin method, these values imply, for a Q_3-approximation, a time step dt equal to 5e−12 s to ensure the stability. If we consider a time step equal to 3 times this minimal value, the number of cells where the condition of stability is locally verified is equal to 535 compared to 13,160 for all the computational domains. Then, only 4% of the cells in the mesh require the application of a local time step equal to dt. The others are evaluated by using a time step equal to 3 dt. If we consider time steps equal to 5 and 7 times dt, the number of cells where dt must be applied increases, respectively, to 25% and 43%.

With a simulation time equal to 3.5e−7 s, we compare the method by using dt as the time step on the whole domain and a strategy of local time steps by using time step given by 3, 5 and 7 times the value of dt. Fig. 13 presents the results obtained in each simulation. We can see the perfect coincidence of the different curves with, for the simulation without local time steps, a CPU time of 337 min 24 s (on a Pentium 4 at 3 GHz) and for the others, a CPU time of 159 min 59 s, 180 min and 194 min 14 s, respectively. In these results, we notice the important gain due to the use of a strategy of local time-stepping. However, this gain is limited by the fact that additional interpolations on cells located around the little cells are introduced in the calculation. This additional cost implies a limit of the time step under which we waste CPU time because the number of small cells considered becomes too large in the mesh. In this example, we can see this effect by using a time step larger than $3 \times 5e{-}12$ s. Nevertheless, in this example, we notice that the CPU time is still smaller than the time required when we do not use a strategy of local time-stepping.

This strategy has also been applied in the case of a larger size example (see Fig. 14) for which a comparison with the classical FDTD method has been done. In this example, an aircraft is illuminated by a plane wave given by ($k_x = 1$, $E_y = 377 * f(t)$, $H_z = f(t)$) with $f(t) = 3.e8 * t - x$. We evaluate the fields at the test-point $A = (6,0,1.5)$ located as shown in Fig. 14. To obtain the same solution, we need to have 6,301,008 cells in the FDTD method and 180,076 in the Galerkin discontinuous method (Q_2-approximation). The amount of memory storage is more interesting in the Galerkin discontinuous method, however, because of the very small size of several cells in our unstructured mesh, we need a very small time step (2.e−12 s) in the Galerkin dis-

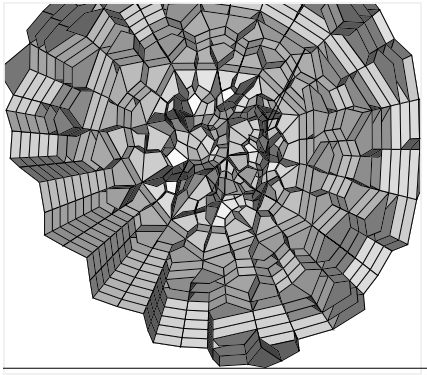

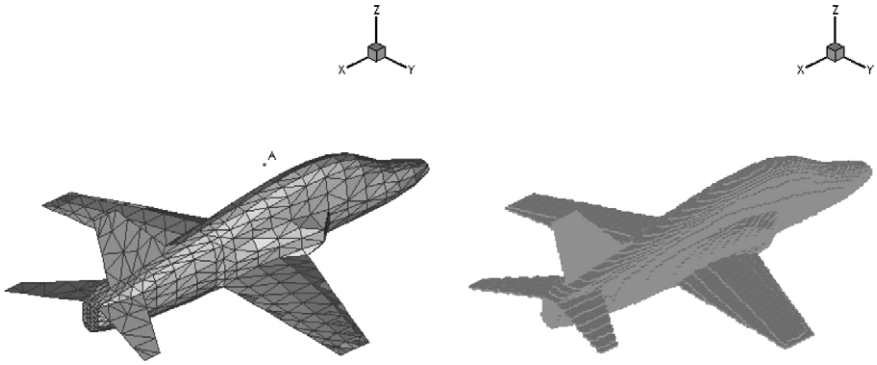

Fig. 14. Discontinuous Galerkin and FDTD surfaces meshing object.

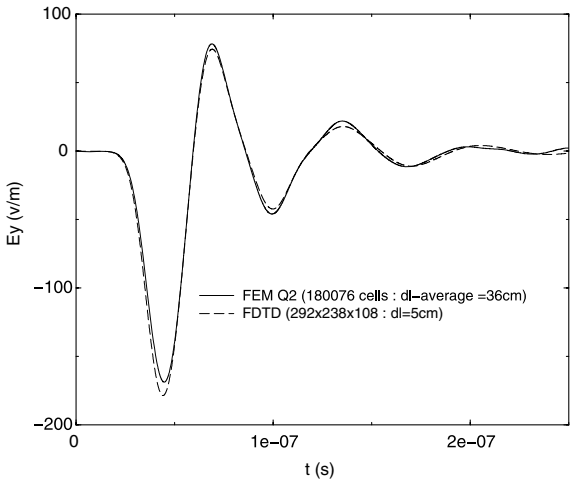

Fig. 15. Comparison between the solutions obtained.

continuous method compared to 8.e−11 s in the FDTD method. In this case, the FDTD is more attractive than the Galerkin discontinuous method in terms of CPU time. Nevertheless, by using the previous local time-stepping strategy, we use only $dt = 2.e{-}12$ s on 18,211 cells (10%) of the mesh and a time step equal to $11dt$ on all the others. In these conditions, the Galerkin discontinuous method is equivalent in terms of CPU time to the FDTD method with a smaller memory storage. In this case, globally, the Galerkin discontinuous method becomes once again more interesting than FDTD. Fig. 15 shows the comparison between the solutions obtained by the two methods.

6. Conclusion

In this paper, we have presented a non-dissipative spatial high order Galerkin discontinuous method to solve the Maxwell equations in the time domain. This method has the advantage of requiring small memory storage with a high order spatial scheme. In particular, the use of a centered formulation allows us to obtain an important gain in storage for jump matrices. A study of the dispersion and the stability of the method has been done and some numerical results have shown the advantage of this method compared to other classical methods such as FDTD, for the same level of accuracy of the solutions. In particular, in our experiments we do not see an error impact due to the spurious modes, on the solution.

However, for complex geometry problems, the drawback to this method is that it requires the use of a mesh composed of hexahedric cells. A solution to obtain this kind of mesh from tetrahedric cells can be easily obtained by splitting each cell into four hexahedric cells. But this implies a significant difference in terms of the size of the cells and the size of the time step which must be very small. A strategy for local time-stepping has been proposed in order to reduce considerably the cost related to the little cells in the mesh. Some examples of scattering for time of observation on at most 100 wavelengths justify the interest of this approach. However, for this method, conservative energy quantity is not ensured and for long time-period the method could be unstable. Then, for some specific examples such as cavities, this strategy could not be efficient and will need to be improved in the future.

References

[1] K.S. Yee, Numerical solution of initial boundary value problems involving Maxwell's equation in isotropic media, IEEE Trans. Antennas Prop. 14 (3) (1966) 302–307.
[2] A. Taflove, S.C. Hagness, Computational Electrodynamics: The Finite-Difference Time-Domain Method, second ed., Artech, Norwood, MA, 2000.
[3] A.C. Cangellaris, D.B. Wright, Analysis of the numerical error caused by the stair-stepped approximation of a conducting boundary in FDTD simulations of electromagnetic phenomena, IEEE Trans. Antennas Prop. AP-39 (10) (1991) 1518–1525.
[4] S.M. Rao, in: D. Irwin (Ed.), Time Domain Electromagnetics, Auburn University Academic Press, 1999.
[5] G. Rodrigue, D. White, A vector finite element time-domain method for solving Maxwell's equations on unstructured hexahedral grids, SIAM J. Sci. Comput. 23 (2001) 683–706.
[6] F. Edelvik, G. Ledfelt, Explicit hybrid time domain solver for the maxwell equations in 3D, J. Sci. Comput. 15 (1) (2000).
[7] K.S. Yee, J.S. Chen, The finite-difference time-domain (FDTD) and the finite-volume time-domain (FVTD) methods in solving Maxwell equation, IEEE Trans. Antennas Prop. 45 (3) (1997) 354–363.
[8] T. Rylander, Stable FEM-FDTD hybrid method for Maxwell's equations, Ph.D. dissertation, Chalmers University of Technology, Goteborg, Sweden, 2002.
[9] X. Ferrieres, J.P. Parmantier, S. Bertuol, A. Ruddle, Application of an hybrid finite difference/finite volume method to solve an automotive EMC problem, IEEE Trans. EMC 46 (4) (2005) 624–634.
[10] S. Pernet, X. Ferrieres, G. Cohen, An original finite element method to solve Maxwell's equations in time domain, in: Proceedings of EMC Zurich' 2003, 18–20 February 2003, Zurich, Switzerland.
[11] G. Cohen, Higher-Order Numerical Methods for Transient Wave Equations, Springer Verlag, Berlin, 2001.
[12] J.S. Hesthavens, T. Warburton, High-order nodal methods on unstructured grids. I. Time-domain solution of Maxwell's equations, J. Comput. Phys. 181 (2002) 1–34.
[13] J. Jin, The Finite Element Method in Electromagnetics, John Wiley & Sons, New York, 1993.
[14] J.-C. Nédélec, Mixed finite elements in $\mathbb{R}^3$, Numer. Math. 35 (3) (1980) 315–341.
[15] J.-C. Nédélec, A new familly of mixed finite elements in $\mathbb{R}^3$, Numer. Math. 50 (1) (1986) 57–81.
[16] G. Cohen, P. Monk, Mur-Nedelec finite element schemes for Maxwell's equations, Comp. Meth. Appl. Mech. Eng. 169 (3–4) (1999) 197–217.
[17] A. Elmkies, P. Joly, Éléments finis d'arête et condensation de masse pour les équations de Maxwell: le cas de la dimension 3, C.R.A.S., Math. 325 (série I) (1997) 1217–1222.
[18] W. Reed, T. Hill, Triangular mesh methods for the neutron transport equation, Tech. Report LA-UR-73-479, Los Alamos National Laboratory, Los Alamos, NM, USA, 1973.
[19] B. Cockburn, G.E. Karniadakis, C.-W. Shu, The Development of Discontiunuous Galerkin MethodsLecture Notes in Computational Science and Engineering, vol. 11, Springer, Berlin, 2000.
[20] P. Houston, I. Perugia, D. Shötzau, Mixed discontinuous Galerkin approximation of the Maxwell operator, SIAM J. Numer. Anal. 42 (1) (2004) 434–459.
[21] I. Perugia, D. Schötzau, P. Monk, Stabilized interior penalty methods for time-harmonic Maxwell equations, Comput. Meth. Appl. Mech. Eng. 191 (2002) 4675–4697.
[22] P. Monk, G.R. Richter, A discontinuous Galerkin method for linear symmetric hyperbolic systems in inhomogeneous media, J. Sci. Comput. 22 (2005) 443–477.
[23] B. Cockburn, F. Li, C.-W. Shu, Locally divergence-free discontinuous Galerkin methods for the Maxwell equations, J. Comput. Phys. 194 (2004) 588–610.
[24] P. Bonnet, X. Ferrieres, Numerical modeling of scattering problems using a time domain finite volume method, JEWA 11 (1997) 1165–1189.
[25] B. Cockburn, F. Li, C.W. Shu, Locally divergence-free discontinuous Galerkin methods for the Maxwell equations, J. Comput. Phys. 194 (2004) 588–610.
[26] S. Piperno, M. Remaki, L. Fezoui, A non-diffusive finite volume scheme for the 3D Maxwell equations on unstructured meshes, SIAM J. Numer. Anal. 39 (6) (2002) 2089–2108.
[27] E. Hairer, S.P. Nørsett, G. Wanner, Solving Ordinary Differential Equations, Springer Series in Computational Mathematics, 1991.

[29] J.P. Berenger, A perfectly matched layer for the absorption of electromagnetic waves, J. Comput. Phys. 114 (1994) 185–200.
[30] K.S. Yee, Time domain extrapolation to the far field based on FDTD calculations, IEEE Trans. Antennas Prop. 39 (3) (1991) 410–413.
[31] W.F. Hall, A.V. Kabakian, A sequence of absorbing boundary conditions for Maxwell's equations, J. Comput. Phys. 194 (2004) 140–155.